The Fermi-LAT high-latitude Survey: Source Count Distributions and the Origin of the Extragalactic Diffuse Background

A. A. Abdo[2,3], M. Ackermann[4], M. Ajello[4,1], E. Antolini[5,6], L. Baldini[7], J. Ballet[8], G. Barbiellini[9,10], D. Bastieri[11,12], B. M. Baughman[13], K. Bechtol[4], R. Bellazzini[7], B. Berenji[4], R. D. Blandford[4], E. D. Bloom[4], E. Bonamente[5,6], A. W. Borgland[4], A. Bouvier[4], J. Bregeon[7], A. Brez[7], M. Brigida[14,15], P. Bruel[16], T. H. Burnett[17], S. Buson[11], G. A. Caliandro[18], R. A. Cameron[4], P. A. Caraveo[19], S. Carrigan[12], J. M. Casandjian[8], E. Cavazzuti[20], C. Cecchi[5,6], Ö. Çelik[21,22,23], E. Charles[4], A. Chekhtman[2,24], C. C. Cheung[2,3], J. Chiang[4], S. Ciprini[6], R. Claus[4], J. Cohen-Tanugi[25], J. Conrad[26,27,28], L. Costamante[4], S. Cutini[20], C. D. Dermer[2], A. de Angelis[29], F. de Palma[14,15], E. do Couto e Silva[4], P. S. Drell[4], R. Dubois[4], D. Dumora[30,31], C. Farnier[25], C. Favuzzi[14,15], S. J. Fegan[16], W. B. Focke[4], Y. Fukazawa[32], S. Funk[4], P. Fusco[14,15], F. Gargano[15], D. Gasparrini[20], N. Gehrels[21], S. Germani[5,6], N. Giglietto[14,15], P. Giommi[20], F. Giordano[14,15], T. Glanzman[4], G. Godfrey[4], I. A. Grenier[8], J. E. Grove[2], S. Guiriec[33], D. Hadasch[34], M. Hayashida[4], E. Hays[21], S. E. Healey[4], D. Horan[16], R. E. Hughes[13], R. Itoh[32], G. Jóhannesson[4], A. S. Johnson[4], T. J. Johnson[21,35], W. N. Johnson[2], T. Kamae[4], H. Katagiri[32], J. Kataoka[36], N. Kawai[37,38], J. Knödlseder[39], M. Kuss[7], J. Lande[4], L. Latronico[7], S.-H. Lee[4], M. Lemoine-Goumard[30,31], M. Llena Garde[26,27], F. Longo[9,10], F. Loparco[14,15], B. Lott[30,31], M. N. Lovellette[2], P. Lubrano[5,6], G. M. Madejski[4], A. Makeev[2,24], M. N. Mazziotta[15], W. McConville[21,35], J. E. McEnery[21,35], C. Meurer[26,27], P. F. Michelson[4], W. Mitthumsiri[4], T. Mizuno[32], C. Monte[14,15], M. E. Monzani[4], A. Morselli[40], I. V. Moskalenko[4], S. Murgia[4], P. L. Nolan[4], J. P. Norris[41], E. Nuss[25], T. Ohsugi[42], N. Omodei[4], E. Orlando[43], J. F. Ormes[41], M. Ozaki[44], D. Paneque[4], J. H. Panetta[4], D. Parent[2,24,30,31], V. Pelassa[25], M. Pepe[5,6], M. Pesce-Rollins[7], F. Piron[25], T. A. Porter[4], S. Rainò[14,15], R. Rando[11,12], M. Razzano[7], A. Reimer[45,4], O. Reimer[45,4], S. Ritz[46], L. S. Rochester[4], A. Y. Rodriguez[18], R. W. Romani[4], M. Roth[17], H. F.-W. Sadrozinski[46], A. Sander[13], P. M. Saz Parkinson[46], J. D. Scargle[47], C. Sgrò[7], M. S. Shaw[4], P. D. Smith[13], G. Spandre[7], P. Spinelli[14,15], J.-L. Starck[8], M. S. Strickman[2], A. W. Strong[43], D. J. Suson[48], H. Tajima[4], H. Takahashi[42], T. Takahashi[44], T. Tanaka[4], J. B. Thayer[4], J. G. Thayer[4], D. J. Thompson[21], L. Tibaldo[11,12,8,49], D. F. Torres[34,18], G. Tosti[5,6], A. Tramacere[4,50,51,1], Y. Uchiyama[4], T. L. Usher[4], V. Vasileiou[22,23], N. Vilchez[39], V. Vitale[40,52], A. P. Waite[4], P. Wang[4], B. L. Winer[13], K. S. Wood[2], Z. Yang[26,27], T. Ylinen[53,54,27], M. Ziegler[46]

[1]Corresponding authors: M. Ajello, majello@slac.stanford.edu; A. Tramacere, tramacer@slac.stanford.edu.

[2]Space Science Division, Naval Research Laboratory, Washington, DC 20375, USA

[3]National Research Council Research Associate, National Academy of Sciences, Washington, DC 20001, USA

[4]W. W. Hansen Experimental Physics Laboratory, Kavli Institute for Particle Astrophysics and Cosmology, Department of Physics and SLAC National Accelerator Laboratory, Stanford University, Stanford, CA 94305, USA

[5]Istituto Nazionale di Fisica Nucleare, Sezione di Perugia, I-06123 Perugia, Italy

[6]Dipartimento di Fisica, Università degli Studi di Perugia, I-06123 Perugia, Italy

[7]Istituto Nazionale di Fisica Nucleare, Sezione di Pisa, I-56127 Pisa, Italy

[8]Laboratoire AIM, CEA-IRFU/CNRS/Université Paris Diderot, Service d'Astrophysique, CEA Saclay, 91191 Gif sur Yvette, France

[9]Istituto Nazionale di Fisica Nucleare, Sezione di Trieste, I-34127 Trieste, Italy

[10]Dipartimento di Fisica, Università di Trieste, I-34127 Trieste, Italy

[11]Istituto Nazionale di Fisica Nucleare, Sezione di Padova, I-35131 Padova, Italy

[12]Dipartimento di Fisica "G. Galilei", Università di Padova, I-35131 Padova, Italy

[13]Department of Physics, Center for Cosmology and Astro-Particle Physics, The Ohio State University, Columbus, OH 43210, USA

[14]Dipartimento di Fisica "M. Merlin" dell'Università e del Politecnico di Bari, I-70126 Bari, Italy

[15]Istituto Nazionale di Fisica Nucleare, Sezione di Bari, 70126 Bari, Italy

[16]Laboratoire Leprince-Ringuet, École polytechnique, CNRS/IN2P3, Palaiseau, France

[17]Department of Physics, University of Washington, Seattle, WA 98195-1560, USA

[18]Institut de Ciencies de l'Espai (IEEC-CSIC), Campus UAB, 08193 Barcelona, Spain

[19]INAF-Istituto di Astrofisica Spaziale e Fisica Cosmica, I-20133 Milano, Italy

[20]Agenzia Spaziale Italiana (ASI) Science Data Center, I-00044 Frascati (Roma), Italy

[21]NASA Goddard Space Flight Center, Greenbelt, MD 20771, USA

[22]Center for Research and Exploration in Space Science and Technology (CRESST) and NASA Goddard Space Flight Center, Greenbelt, MD 20771, USA

[23]Department of Physics and Center for Space Sciences and Technology, University of Maryland Baltimore County, Baltimore, MD 21250, USA

[24]George Mason University, Fairfax, VA 22030, USA

[25]Laboratoire de Physique Théorique et Astroparticules, Université Montpellier 2, CNRS/IN2P3, Mont-

pellier, France

[26]Department of Physics, Stockholm University, AlbaNova, SE-106 91 Stockholm, Sweden

[27]The Oskar Klein Centre for Cosmoparticle Physics, AlbaNova, SE-106 91 Stockholm, Sweden

[28]Royal Swedish Academy of Sciences Research Fellow, funded by a grant from the K. A. Wallenberg Foundation

[29]Dipartimento di Fisica, Università di Udine and Istituto Nazionale di Fisica Nucleare, Sezione di Trieste, Gruppo Collegato di Udine, I-33100 Udine, Italy

[30]CNRS/IN2P3, Centre d'Études Nucléaires Bordeaux Gradignan, UMR 5797, Gradignan, 33175, France

[31]Université de Bordeaux, Centre d'Études Nucléaires Bordeaux Gradignan, UMR 5797, Gradignan, 33175, France

[32]Department of Physical Sciences, Hiroshima University, Higashi-Hiroshima, Hiroshima 739-8526, Japan

[33]Center for Space Plasma and Aeronomic Research (CSPAR), University of Alabama in Huntsville, Huntsville, AL 35899, USA

[34]Institució Catalana de Recerca i Estudis Avançats (ICREA), Barcelona, Spain

[35]Department of Physics and Department of Astronomy, University of Maryland, College Park, MD 20742, USA

[36]Research Institute for Science and Engineering, Waseda University, 3-4-1, Okubo, Shinjuku, Tokyo, 169-8555 Japan

[37]Department of Physics, Tokyo Institute of Technology, Meguro City, Tokyo 152-8551, Japan

[38]Cosmic Radiation Laboratory, Institute of Physical and Chemical Research (RIKEN), Wako, Saitama 351-0198, Japan

[39]Centre d'Étude Spatiale des Rayonnements, CNRS/UPS, BP 44346, F-30128 Toulouse Cedex 4, France

[40]Istituto Nazionale di Fisica Nucleare, Sezione di Roma "Tor Vergata", I-00133 Roma, Italy

[41]Department of Physics and Astronomy, University of Denver, Denver, CO 80208, USA

[42]Hiroshima Astrophysical Science Center, Hiroshima University, Higashi-Hiroshima, Hiroshima 739-8526, Japan

[43]Max-Planck Institut für extraterrestrische Physik, 85748 Garching, Germany

[44]Institute of Space and Astronautical Science, JAXA, 3-1-1 Yoshinodai, Sagamihara, Kanagawa 229-8510, Japan

[45]Institut für Astro- und Teilchenphysik and Institut für Theoretische Physik, Leopold-Franzens-Universität Innsbruck, A-6020 Innsbruck, Austria

[46]Santa Cruz Institute for Particle Physics, Department of Physics and Department of Astronomy and Astrophysics, University of California at Santa Cruz, Santa Cruz, CA 95064, USA

[47]Space Sciences Division, NASA Ames Research Center, Moffett Field, CA 94035-1000, USA

majello@slac.stanford.edu

ABSTRACT

This is the first of a series of papers aimed at characterizing the populations detected in the high-latitude sky of the *Fermi*-LAT survey. In this work we focus on the intrinsic spectral and flux properties of the source sample. We show that when selection effects are properly taken into account, *Fermi* sources are on average steeper than previously found (e.g. in the bright source list) with an average photon index of 2.40±0.02 over the entire 0.1–100 GeV energy band. We confirm that FSRQs have steeper spectra than BL Lac objects with an average index of 2.48±0.02 versus 2.18±0.02. Using several methods we build the deepest source count distribution at GeV energies deriving that the intrinsic source (i.e. blazar) surface density at $F_{100} \geq 10^{-9}$ ph cm^{-2} s^{-1} is $0.12^{+0.03}_{-0.02}$ deg^{-2}. The integration of the source count distribution yields that point sources contribute 16(±1.8) % (±7 % systematic uncertainty) of the GeV isotropic diffuse background. At the fluxes currently reached by LAT we can rule out the hypothesis that point-like sources (i.e. blazars) produce a larger fraction of the diffuse emission.

Subject headings: cosmology: observations – diffuse radiation – galaxies: active gamma rays: diffuse background – surveys – galaxies: jets

1. Introduction

The origin of the extragalactic gamma-ray background (EGB) at GeV γ-rays is one of the fundamental unsolved problems in astrophysics. The EGB was first detected by the SAS-

[48]Department of Chemistry and Physics, Purdue University Calumet, Hammond, IN 46323-2094, USA

[49]Partially supported by the International Doctorate on Astroparticle Physics (IDAPP) program

[50]Consorzio Interuniversitario per la Fisica Spaziale (CIFS), I-10133 Torino, Italy

[51]INTEGRAL Science Data Centre, CH-1290 Versoix, Switzerland

[52]Dipartimento di Fisica, Università di Roma "Tor Vergata", I-00133 Roma, Italy

[53]Department of Physics, Royal Institute of Technology (KTH), AlbaNova, SE-106 91 Stockholm, Sweden

[54]School of Pure and Applied Natural Sciences, University of Kalmar, SE-391 82 Kalmar, Sweden

2 mission (Fichtel et al. 1975) and its spectrum was measured with good accuracy by the Energetic Gamma Ray Experiment Telescope (EGRET Sreekumar et al. 1998; Strong et al. 2004) on board the Compton Observatory. These observations by themselves do not provide much insight into the sources of the EGB.

Blazars, active galactic nuclei (AGN) with a relativistic jet pointing close to our line of sight, represent the most numerous population detected by EGRET Hartman et al. (1999) and their flux constitutes 15 % of the total EGB intensity (resolved sources plus diffuse emission). Therefore, undetected blazars (e.g. all the blazars under the sensitivity level of EGRET) are the most likely candidates for the origin of the bulk of the EGB emission. Studies of the luminosity function of blazars showed that the contribution of blazars to the EGRET EGB could be in the range from 20 % to 100 % (e.g. Stecker & Salamon 1996; Chiang & Mukherjee 1998; Mücke & Pohl 2000), although the newest derivations suggest that blazars are responsible for only $\sim$ 20–40 % of the EGB (e.g. Narumoto & Totani 2006; Dermer 2007; Inoue & Totani 2009).

It is thus possible that the EGB emission encrypts in itself the signature of some of the most powerful and interesting phenomena in astrophysics. Intergalactic shocks produced by the assembly of Large Scale Structures (e.g. Loeb & Waxman 2000; Miniati 2002; Keshet et al. 2003; Gabici & Blasi 2003), γ-ray emission from galaxy clusters (e.g. Berrington & Dermer 2003; Pfrommer et al. 2008), emission from starburst as well as normal galaxies (e.g. Pavlidou & Fields 2002; Thompson et al. 2007), are among the most likely candidates for the generation of diffuse the GeV emission. Dark matter (DM) which constitutes more than 80 % of the matter in the Universe can also provide a diffuse, cosmological, background of γ-rays. Indeed, supersymmetric theories with R-parity predict that the lightest DM particles (i.e., the neutralinos) are stable and can annihilate into GeV γ-rays (e.g. Jungman et al. 1996; Bergström 2000; Ullio et al. 2002; Ahn et al. 2007).

With the advent of the *Fermi* Large Area Telescope (LAT) a better understanding of the origin of the GeV diffuse emission becomes possible. *Fermi* has recently performed a new measurement of the EGB spectrum (also called isotropic diffuse background, Abdo et al. 2010d). This has been found to be consistent with a featureless power law with a photon index of $\sim$2.4 in the 0.2–100 GeV energy range. The integrated flux (E$\geq$100 MeV) of $1.03(\pm0.17) \times 10^{-5}$ ph cm^{-2} s^{-1} sr^{-1} has been found to be significantly lower than the one of $1.45(\pm0.05)\times10^{-5}$ ph cm^{-2} s^{-1} sr^{-1} determined from EGRET data (see Sreekumar et al. 1998).

In this study we address the contribution of *unresolved* point sources to the GeV diffuse emission and we discuss the implications. Early findings on the integrated emission of *unresolved* blazars were already reported in Abdo et al. (2009a) using a sample of bright

AGN detected in the first three months of *Fermi* observations. The present work represents a large advance, with ∼4 times more blazars and a detailed investigation of selection effects in source detection.

This work is organized as follows. In § 3 the intrinsic spectral properties of the *Fermi* sources are determined. In § 4 the Monte Carlo simulations used for this analyses are outlined with the inherent systematic uncertainties (see § 5). Finally the source counts distributions are derived in § 6 and § 7 while the contribution of point sources to the GeV diffuse background is determined in § 8. § 9 discusses and summarizes our findings. Since the final goal of this work is deriving the contribution of sources to the EGB, we will only use physical quantities (i.e. source flux and photon index) averaged over the time (11 months) included in the analysis for the First *Fermi*-LAT catalog (1FGL, Abdo et al. 2010b).

2. Terminology

Throughout this paper we use a few terms which might not be familiar to the reader. In this section meanings of the most often used are clarified.

- *spectral bias*: (or photon index bias) is the selection effect which allows *Fermi*-LAT to detect spectrally hard sources at fluxes generally fainter than for soft sources.
- *flux-limited* sample: it refers to a sample which is selected uniformly according solely to the source flux. If the flux limit is chosen to be bright enough (as in the case of this paper), then the selection effects affecting any other properties (e.g. the source spectrum) of the sample are negligible. This is a truly uniformly selected sample.
- *diffuse emission from unresolved point sources*: it represents a measurement of the integrated emission from sources which have not been detected by *Fermi*. As it will be shown in the next sections, for each source detected at low fluxes, there is a large number of sources which have not been detected because of selection effects (e.g. the local background was too large or the photon index was too soft, or a combination of both). The diffuse emission from *unresolved* point sources (computed in this work) addresses the contribution of all those sources which have not been detected because of these selection effects, but have a flux which is formally larger than the faintest *detected* source.

3. Average Spectral Properties

3.1. Intrinsic Photon index distributions

As shown already in (Abdo et al. 2009a, but see also Fig. 1), at faint fluxes the LAT detects more easily hard-spectrum sources rather than sources with a soft spectrum. Sources with a photon index (e.g. the exponent of the power-law fit to the source photon spectrum) of 1.5 can be detected to fluxes which are a factor > 20 fainter than those at which a source with a photon index of 3.0 can be detected (see Abdo et al. 2010e, for details). Thus, given this strong selection effect, the intrinsic photon index distribution is necessarily different from the observed one. An approach to recover the intrinsic photon index distribution is obtained by studying the sample above $F_{100} \approx 7 \times 10^{-8}$ ph cm^{-2} s^{-1} and $|b| \geq 10°$ (see right panel of Fig. 1). Indeed above this flux limit, LAT detects all sources irrespective of their photon index, flux or position in the high-latitude sky. Above this limit LAT detects 135 sources. Their photon index distribution, reported in Fig. 1 is compatible with a Gaussian distribution with mean of 2.40±0.02 and dispersion of 0.24±0.02. These values differ from the mean of 2.23±0.01 and dispersion of 0.33±0.01 derived using the entire $|b| \geq 10°$ sample. Similarly the intrinsic photon-index distributions of FSRQs and BL Lacs are different from the observed distributions. In both case the *observed* average photon-index is harder than the intrinsic average value. The results are summarized in Tab. 1.

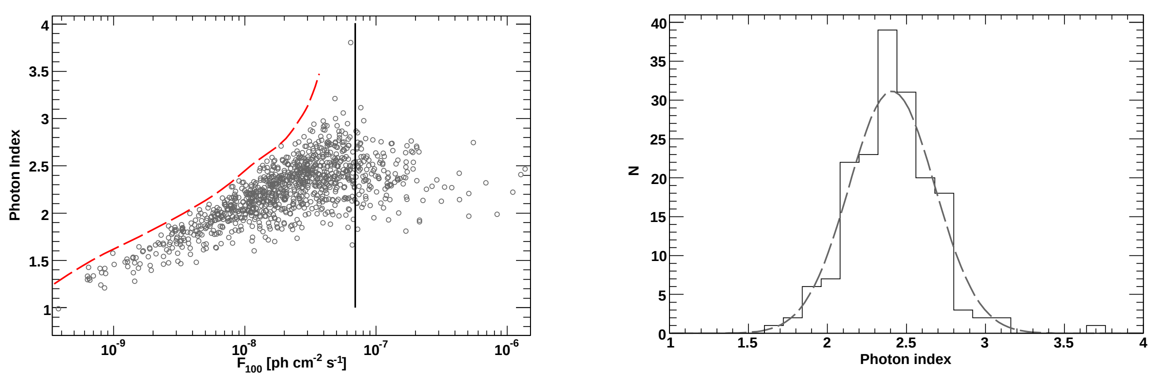

Fig. 1.— **Left Panel:**Flux-photon index plane for all the $|b| \geq 10°$ sources with TS≥ 25. The dashed line is the flux limit as a function of photon index reported in Abdo et al. (2010e), while the solid line represents the limiting flux above which the spectral selection effects become negligible. **Right Panel:** Photon index distribution of all sources for $F_{100} \geq 7\times10^{-8}$ ph cm^{-2} s^{-1}. Above this limit the LAT selection effect towards hard sources becomes negligible.

3.2. Stacking Analysis

Another way to determine the average spectral properties is by stacking source spectra together. This is particularly simple since (Abdo et al. 2010b) reports the source flux in five different energy bands. We thus performed a stacking analysis of those sources with $F_{100} \geq 7 \times 10^{-8}$ ph cm^{-2} s^{-1}, TS$\geq$ 25, and $|b| \geq 10°$. For each energy band the average flux is computed as the weighted average of all source fluxes in that band using the inverse of the flux variance as a weight. The average spectrum is shown in Fig. 2. A power law model gives a satisfactory fit to the data (e.g. $\chi^2/dof \approx 1$), yielding a photon index of 2.41±0.07 in agreement with the results of the previous section.

We repeated the same exercise separately for sources identified as FSRQs and BL Lacs in the *flux-limited* sample. Both classes have an average spectrum which is compatible with a single power law over the whole energy band. FSRQs are characterized by an index of 2.45±0.03 while BL Lac objects have an average index of 2.23±0.03

4. Monte Carlo Simulations

In order to estimate the LAT sky coverage robustly we performed detailed Monte Carlo simulations. The scheme of the simulation procedure is an improved version of what has already been applied in Abdo et al. (2009a). We performed 18 end-to-end simulations of the LAT sky which resemble as closely as possible the observed one. The tool *gtobssim*[1] has been used for this purpose. For each simulation we modeled the Galactic and isotropic diffuse

[1]The list of science tools for the analysis of *Fermi* data is accessible at http://fermi.gsfc.nasa.gov/ssc/data/analysis/scitools/overview.html.

Table 1. Observed versus Intrinsic photon indices distributions for the Fermi/LAT source classes.

	Observed Distribution		Intrinsic Distribution	
SAMPLE	mean	σ	mean	σ
ALL	2.24±0.01	0.31±0.01	2.40±0.02	0.24±0.02
FSRQ	2.44±0.01	0.21±0.01	2.47±0.02	0.19±0.02
BL Lac	2.05±0.02	0.29±0.01	2.20±0.04	0.22±0.03

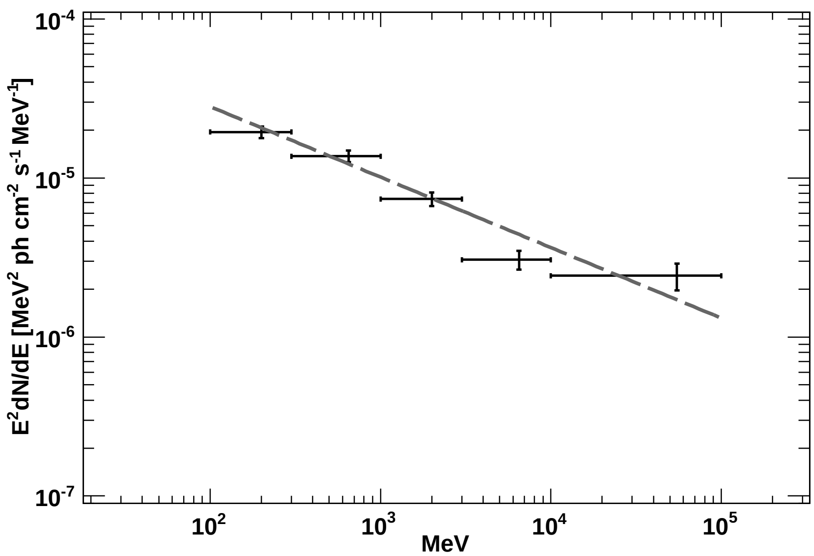

Fig. 2.— Stacked spectrum of sources in the *flux-limited* sample. The dashed line is the best power law fit with a slope of 2.41±0.07.

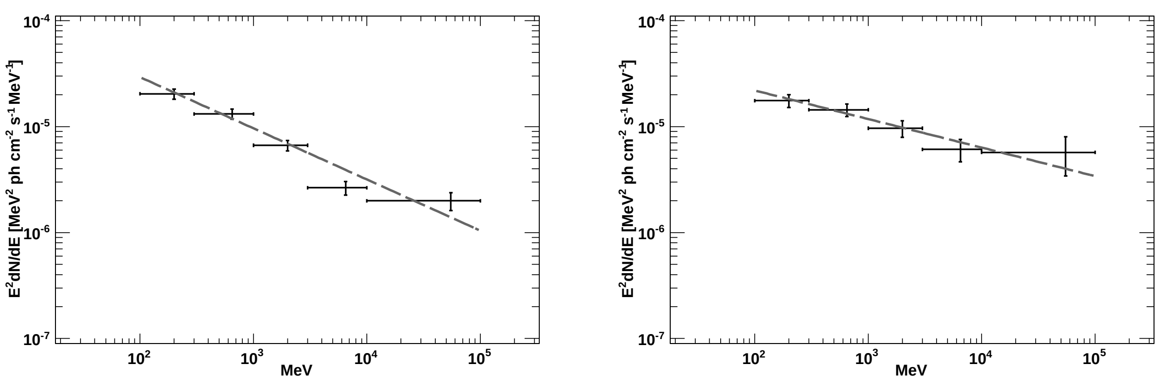

Fig. 3.— Stacked spectrum of FSRQs (left) and BL Lac objects (right) in the *Fermi*-LAT *flux-limited* sample.

backgrounds using models (e.g. gll_iem_v02.fit) currently recommended by the LAT team.

An isotropic population of point-like sources was added to each simulated observation. The coordinates of each source were randomly drawn in order to produce an isotropic distribution on the sky. Source fluxes were randomly drawn from a standard log N–log S distribution with parameters similar to the one observed by LAT (see next section). Even though the method we adopt to derive the survey sensitivity does not depend on the normalization or the slope of the input log N–log S, using the real distribution allows simulated observations to be produced that closely resemble the sky as observed with the LAT. The photon index of each source was also drawn from a Gaussian distribution with mean of 2.40 and $1\,\sigma$ width of 0.28. As noted in the previous section, this distribution represents well the intrinsic (not the observed one) distribution of photon indices. The adopted dispersion is slightly larger than what was found in the previous section and it is derived from the analysis of the entire sample (see § 6.2). In this framework we are neglecting any possible dependence of the photon index distribution with flux. Also we remark that the approach used here to derive the source count distribution depends very weakly on the assumptions (e.g. the log N–log S used) made in the simulations.

More than 45000 randomly distributed sources have been generated for each realization of the simulations. Detection follows (albeit in a simpler way) the scheme used in Abdo et al. (2010b). This scheme adopts three energy bands for source detection. The first band includes all *front*-converting[2] and *back*-converting photons with energies larger than 200 MeV and 400 MeV, respectively. The second band starts at 1 GeV for *front* photons and at 2 GeV for *back* photons. The high-energy band starts at 5 GeV for *front* photons and at 10 GeV for *back* photons. The choice of combining *front* and *back* events with different energies is motivated by the fact that *front* events have a better point spread function (PSF) than *back* ones. The two PSFs are similar when the energy of *back*-converting photons is approximately twice as that of *front*-converting ones. The image pixel sizes changes according to the energy band and is 0.1, 0.2 and 0.3 degrees for the low, medium and high-energy bands respectively. The final list of *candidate* sources is obtained starting the detection at the highest energy band and adding all those sources which, being detected at lower energy, have a position not consistent with those detected at high energy. The detection step uses *pgwave* for determining the position of the excesses and *pointfit* for refining the source position. *Pgwave* (Ciprini et al. 2007) is a tool which uses several approaches (e.g. wavelets, thresholding, image denoising and a sliding cell algorithm) to find source candidates while *pointfit* (e.g. Burnett et al. 2009) employes a simplified binned likelihood algorithm to optimize the source position.

All the source candidates found at this stage are then ingested to the Maximum Likelihood (ML) algorithm *gtlike* to determine the significance and the spectral parameters. In this step all sources' spectra are modeled as single power laws. On average, for each simulation only ∼1000 sources are detected (out of the 45000 simulated ones) above a TS[3] of 25

---

[2]Photons pair-converting in the top 12 layers of the tracker are classified as *front*-converting photons or *back*-converting otherwise.

[3]The test statistics (or TS) is defined as: TS$=-2(\ln L_0 - \ln L_1)$. Where L_0 and L_1 are the likelihoods of

and this is found to be in good agreement with the real data.

4.1. Performances of the detection algorithm on real data

In order to test the reliability of our detection pipeline we applied it the to real 1 year dataset. Our aim was to cross check our result with the result reported in Abdo et al. (2010b). The flux above 100 MeV, computed from the power-law fit to the 100 MeV–100 GeV data, is not reported in Abdo et al. (2010b), but it can be readily obtained using the following expression:

$$F_{100} = E_{piv} \times F_{density} \times \left(\frac{100}{E_{piv}}\right)^{1-\Gamma} \times |1-\Gamma|^{-1}, \qquad (1)$$

where F_{100} is the 100 MeV–100 GeV photon flux, Γ is the absolute value of the photon index, E_{piv} is the pivot energy and $F_{density}$ is the flux density at the pivot energy (see Abdo et al. 2010b, for details). Fig. 4 shows the comparisons of both fluxes (above 100 MeV) and of the photon indices for the sources detected in both pipelines. It is clear that the fluxes and photon indices derived in this analysis are reliable; for each source they are consistent with those in Abdo et al. (2010b) within the reported errors.

The number of sources detected in the simplified pipeline is smaller than found by Abdo et al. (2010b). Above a TS of 50 and $|b| \geq 20^{\circ}$ our approach detects 425 sources while the 1FGL catalog has 497. Indeed, our aim is not to produce a detection algorithm which is as sensitive than the one used in Abdo et al. (2010b), but a detection algorithm which is proven to be reliable and can be applied consistently to both real data and simulations. This allows us to assess properly all selection effects important for the LAT survey and its analysis. On this note we remark that all the 425 sources detected by our pipeline are also detected by Abdo et al. (2010b). For this reason we limit the studies presented in this work to the subsample of sources which is detected by our pipeline. The details of this sample of sources are reported in Tab. 2. The associations are the ones reported in Abdo et al. (2010e) and Abdo et al. (2010b). In our sample 161 sources are classified as FSRQs and 163 as BL Lac objects while only 4 as blazars of uncertain classification. The number of sources which are unassociated is 56, thus the identification incompleteness of this sample is ∼13%.

---

the background (null hypothesis) and the hypothesis being tested (e.g. source plus background). According to Wilks (1938), the significance of a detection is approximately $n_{\sigma} = \sqrt{(TS)}$ (see also Ajello et al. 2008).

Table 2. Composition of the |b| ≥20 TS≥50 sample used in this analysis.

CLASS	# objects
Total	425
FSRQs	161
BL Lacs	163
Uncertain[a]	4
Blazar Candidates	24
Radio Galaxies	2
Pulsars	9
Others[b]	6
Unassociated sources	56

[a]Blazars with uncertain classification.

[b]It includes Starburst galaxies, Narrow line Seyfert 1 objects and Seyfert galaxy candidates.

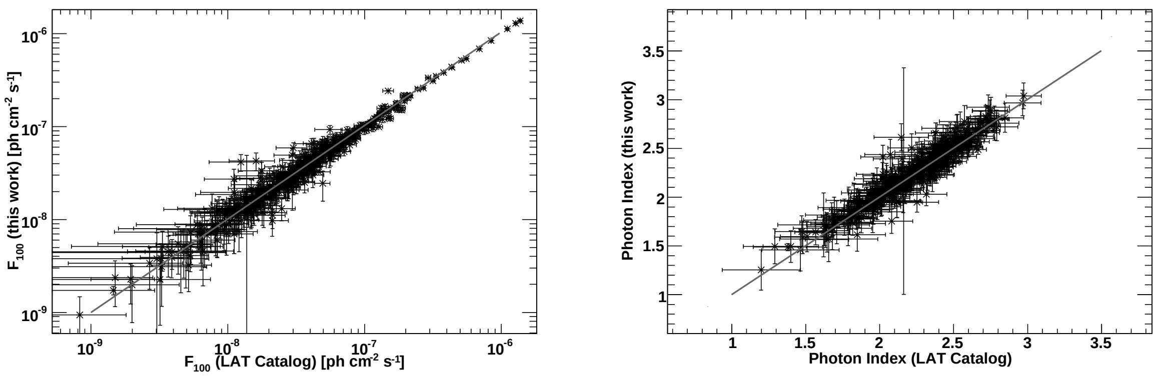

Fig. 4.— Performance of the detection pipeline used in this work with respect to the detection pipeline used in Abdo et al. (2010b). The left panel shows the comparison of the reconstructed γ-ray fluxes while the right panel shows the comparison of the photon indices. In both cases the solid line shows the the locus of points for which the quantity reported in the y-axis equals the one in the x-axis.

4.2. Derivation of the Sky Coverage

In order to derive the sky coverage from simulations, detected sources (output) need to be associated to the simulated ones (input). We do this on a statistical basis using an estimator which is defined for each set of input-output sources as:

$$R^2 = \left(\frac{||\bar{x} - \bar{x_0}||}{\sigma_{pos}}\right)^2 + \left(\frac{S - S_0}{\sigma_S}\right)^2 + \left(\frac{\Gamma - \Gamma_0}{\sigma_\Gamma}\right)^2 \tag{2}$$

where $\bar{x}$, S and Γ are the source coordinates, fluxes and photon indices as determined from the ML step while $\bar{x_0}$, S_0 and Γ_0 are the simulated (input) values. The $1\,\sigma$ errors on the position, flux and photon index are σ_{pos}, σ_S and σ_Γ respectively. We then flagged as the most likely associations those pairs with the minimum value of R^2. All pairs with an angular separation which is larger than the $4\,\sigma$ error radius are flagged as spurious and excised from the following analysis. The empirical, as derived from the real data, $5\,\sigma$ error radius as a function of source TS is shown in Fig. 5. As in Hasinger et al. (1993) and in Cappelluti et al. (2007) we defined *confused* sources for which the ratio $S/(S_0 + 3\sigma_S)$ (where σ_S is the error on the output flux) is larger than 1.5. We found that, according to this criterion, $\sim$4 % of the sources (detected for $|b| \geq 10°$) are confused in the first year survey.

The right panel of Fig. 6 shows the ratio of reconstructed to simulated source flux versus the simulated source flux. At medium to bright fluxes the distribution of the ratio is centered on unity showing that there are no systematic errors in the flux measurement. At low fluxes (in particular for $F_{100} < 10^{-9}$ ph cm^{-2} s^{-1}) the distribution is slightly (or somewhat) biased toward values greater than unity. This is produced by three effects: 1) source confusion, 2) Eddington bias (Eddington 1940) and 3) non converging Maximum Likelihood fits (see § 5.1 for details). The Eddington bias arises from measurement errors of any intrinsic source property (e.g. source flux). Given its nature, it affects only sources close to the detection threshold. Indeed, at the detection threshold the uncertainty in the reconstructed fluxes makes sources with a measured flux slightly larger than the real value more easily detectable in the survey rather than those with a measured flux slightly lower than the real one. This causes the shift of the flux ratio distribution of Fig. 6 to move systematically to values larger than unity at low fluxes. In any case, the effect of this bias is not relevant as it affects less than 1 % of the entire population. This uncertainty will be neglected as only sources with $F_{100} \geq 10^{-9}$ ph cm^{-2} s^{-1} will be considered for the analysis presented here. Moreover, the right panel of Fig. 6 shows that the measured photon index agrees well with the simulated one.

In addition to assessing the reliability and biases of our source detection procedure, the main aim of these simulations is to provide a precise estimate of the completeness function of the *Fermi*/LAT survey (known also as sky coverage). The one-dimensional sky coverage can be derived for each bin of flux as the ratio between the number of detected sources and the number of simulated sources. The detection efficiency for the entire TS$\geq$ 50 and $|b| \geq 20^{\circ}$ sample is reported in Fig. 7. This plot shows that the LAT sensitivity extends all the way to $F_{100} \sim 10^{-10}$ ph cm^{-2} s^{-1} although at those fluxes only the hardest sources can be detected. Also the sample becomes complete for $F_{100} = 7 - 8 \times 10^{-8}$ ph cm^{-2} s^{-1}. Since for these simulations, the *intrinsic* distribution of photon indices has been used (see e.g. § 3.1) this sky coverage takes properly into account the bias towards the detection of hard sources. This also means that this sky coverage cannot be applied to other source samples with very different photon index distributions.

5. Systematic Uncertainties

5.1. Non converging Maximum Likelihood fits

A small number of sources detected by our pipeline have unreliable spectral fits. Most of the time, these sources have a reconstructed photon index which is very soft (e.g. ∼5.0) and at the limit of the accepted range of values. As a consequence their reconstructed flux overestimates the true flux by up to factor 1000 (see left panel of Fig. 6). This is due to the fact the the ML algorithm does not find an absolute minimum of the fitting function for these cases. Inspection of the regions of interests (ROIs) of these objects shows that this

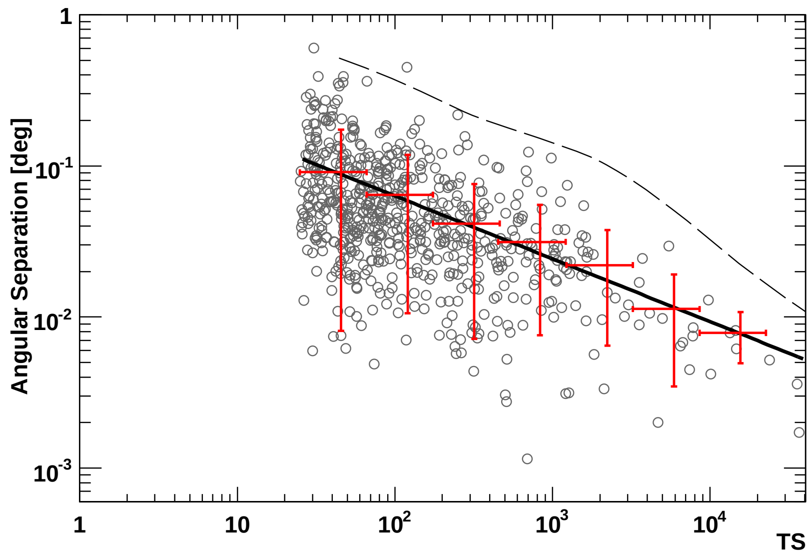

Fig. 5.— Angular separation of the real LAT sources from the most probable associated counterpart as a function of TS. All sources with $|b| \geq 10°$ with a probability of associations larger than 0.5 were used (see Abdo et al. 2010e, for a definition of probability of association). The solid line is the best fit for the mean offset of the angular separations while the dashed line represents the observed $5\,\sigma$ error radius as a function of test statistics. Note that the $5\,\sigma$ error radius is weakly dependent on the level of probability of association chosen.

tends to happen either in regions very dense with sources or close to the Galactic plane, where the diffuse emission is the brightest. The best approach in this case would be to adopt an iterative procedure for deriving the best-fitting parameters which starts by optimizing the most intense components (e.g. diffuse emissions and bright sources) and then move to the fainter ones. This procedure is correctly implemented in Abdo et al. (2010b). Its application to our problem would make the processing time of our simulations very long and we note that the systematic uncertainty deriving from it is small. Indeed, the number of sources with unreliable spectral parameters are for $TS \geq 25$ are 2.3 % and 2.0 % for $|b| \geq 15°$ a $|b| \geq 20°$ respectively. These fractions decrease to 1.2 % and 0.9 % adopting TS$\geq$ 50.

To limit the systematic uncertainties in this analysis, we will thus select only those sources which are detected above TS$\geq$ 50 and $|b| \geq 20°$. It will also be shown that results do not change if the sample is enlarged to include all sources with $|b| \geq 15°$.

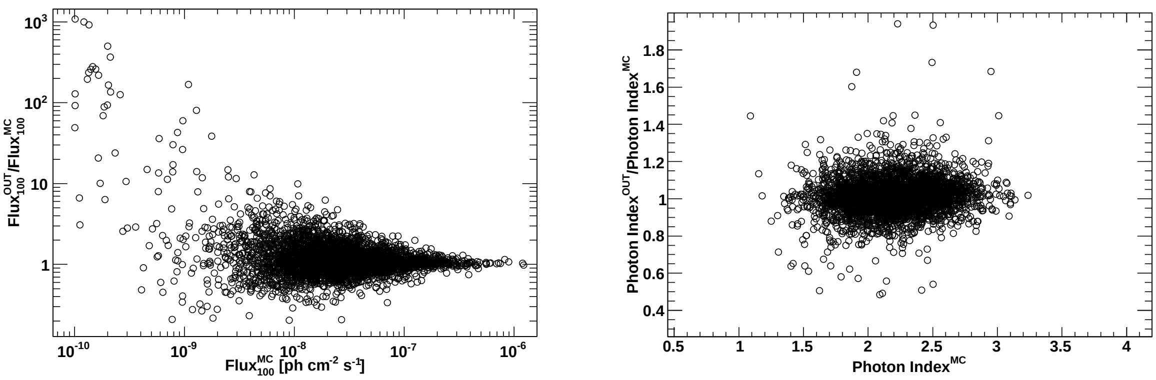

Fig. 6.— Left Panel: Reconstructed versus Simulated fluxes for all sources with TS≥50 and $|b|$ ≥20°. For the analysis reported here only sources with $F_{100} \geq 10^{-9}$ ph cm^{-2} s^{-1} are considered. Right Panel: Reconstructed versus Simulated photon indices for all sources with TS≥50 and $|b|$ ≥20°.

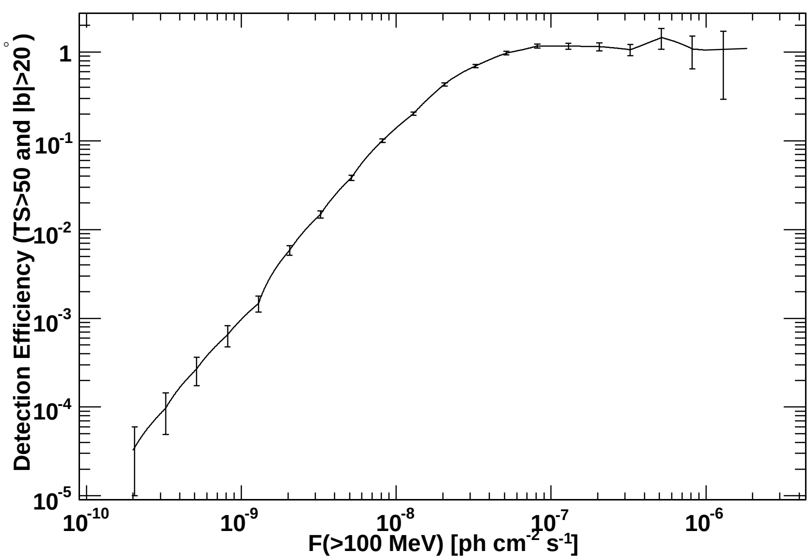

Fig. 7.— Detection efficiency as a function of measured source flux for $|b| \geq 20°$, TS≥ 50 and for a sample of sources with a mean photon index of 2.40 and dispersion of 0.28. The error bars represent statistical uncertainties from the counting statistic of our Monte Carlo simulations.

5.2. Variability

It is well known that blazars are inherently variable objects with variability in flux of up to a factor 10 or more. Throughout this work only average quantities (i.e. mean flux and mean photon index) are used. This is correct in the context of the determination of the mean energy release in the Universe of each source. Adopting the peak flux (i.e. the brightest flux displayed by each single source) would produce the net effect of overestimating the true intrinsic source density at any flux (see the examples in Reimer & Thompson 2001) with the result of overestimating the contribution of sources to the diffuse background.

It is not straightforward to determine how blazar variability affects the analysis presented here. On timescales large enough (such as the one spanned by this analysis), the mean flux is a good estimator of the mean energy release of a source. This is not true anymore on short timescales (e.g. $\sim$1 month) since the mean flux corresponds to the source flux at the moment of the observation. The continuous scanning of the γ-ray sky performed by *Fermi* allows to determine long-term variability with unprecedented accuracy. As shown already in Abdo et al. (2009a) the picture arising from *Fermi* is rather different from the one derived by EGRET (Hartman et al. 1999). Indeed, the peak-to-mean flux ratio for *Fermi* sources is considerably smaller than for EGRET sources. For most of the *Fermi* sources this is just a factor 2, as is confirmed in the 1 year sample (see Fig.10 in Abdo et al. 2010e). This excludes the possibility that most of the sources are detected because of a single outburst which happened during the 11 months of observation and are undetected for the remaining time. Moreover, as shown in Abdo et al. (2010c) there is little or no variation of the photon index with flux. We thus believe that no large systematic uncertainties are derived from the use of average physical quantities and the total systematic uncertainty (see next section) will be slightly overestimated to accommodate possible uncertainties caused by variability.

5.3. Non power law spectra

It is well known that the spectra of blazars are complex and often show curvature when analyzed over a large waveband. In this case the approximation of their spectrum with a simple power law (in the 0.1–100 GeV band) might provide a poor estimate of their true flux. To estimate the uncertainties derived by this assumption we plotted for the extragalactic sample used here (e.g. TS$\geq$ 50 and $|b| \geq 20°$) the source flux as derived from the power-law fit to the whole band versus the source flux as derived from the sum of the fluxes over the 5 energy bands reported in Abdo et al. (2010b). This comparison is reported in Fig. 8. From the figure it is apparent that the flux (F_{100}) derived from a power-law fit to the whole band overestimates slightly the true source flux. Analysis of the ratio between the power-law flux and flux derived in 5 energy bands, shows that on average the F_{100} flux overestimates the true source flux by ∼8 %. At very bright fluxes (e.g. $F_{100} \geq 10^{-7}$ ph cm^{-2} s^{-1}) the overestimate reduces to ∼5 %. For the analysis presented here we will thus assume that the total systematic uncertainty connected to the use of fluxes computed with a power-law fit over the broad 0.1–100 GeV band is 8 %.

Considering also the uncertainties of the previous sections, we derive that the total systematic uncertainty for the sample used here (TS≥50 and $|b| \geq 20°$) is ∼10 %. Since this uncertainty affects mostly the determination of the source flux it will be propagated by shifting in flux the sky coverage of Fig.7 by ±10 %.

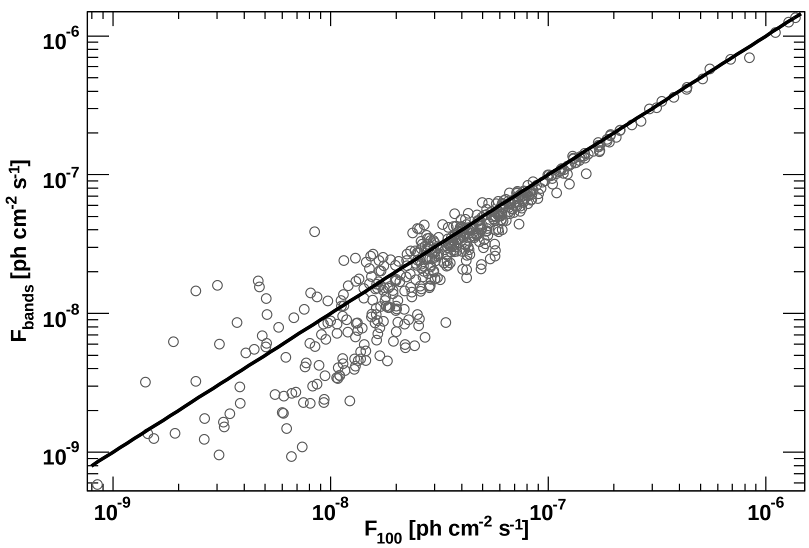

Fig. 8.— Source flux estimated with a power-law fit to the 0.1–100 GeV band versus the sum of the source fluxes derived in 5 contiguous energy bands (see Abdo et al. 2010b, for details). The solid line is the F_{bands}=F_{100} relation. The spread at low fluxes arises from the difficulties of estimating the source flux in small energy bands.

6. Source Counts Distributions

The source counts distribution, commonly referred to as log N–log$S$ or size distribution, is the cumulative number of sources $N(> S)$ detected above a given flux S. In this section we apply several methods to derive the source count distribution of *Fermi*/LAT sources. We also remark that the catalog used for this analysis is the one described in § 4.1 (see also

Tab. 2).

6.1. Standard Approach

A standard way to derive the (differential) log N–log S is through the following expression:

$$\frac{dN}{dS} = \frac{1}{\Delta\ S} \sum_{i=1}^{N_{\Delta S}} \frac{1}{\Omega_i} \tag{3}$$

where $N_{\Delta S}$ is the total number of detected sources with fluxes in the ΔS interval, and Ω_i is the solid angle associated with the flux of the i_{th} source (i.e., the detection efficiency multiplied by the survey solid angle). We also note that formally N is an areal density and should be expressed as $dN/d\Omega$. However for simplicity of notation the areal density will, throughout this paper, be expressed as N. For the $|b| \geq 20°$ sample the geometric solid angle of the survey is 27143.6 deg^2. In each flux bin, the final uncertainty is obtained by summing in quadrature the error on the number of sources and the systematic uncertainties described in § 5.

Both the differential and the cumulative version of the source count distributions are reported in Fig. 9. In order to parametrize the source count distribution we perform a χ^2 fit to the differential data using a broken power-law model of the type:

$$\begin{aligned} \frac{dN}{dS} &= AS^{-\beta_1} \qquad\qquad S \geq S_b \\ &= AS_b^{-\beta_1+\beta_2} S^{-\beta_2} \quad S < S_b \end{aligned} \tag{4}$$

where A is the normalization and S_b is the flux break. The best-fit parameters are reported in Tab. 3. The log N– log S distribution of GeV sources shows a strong break ($\Delta\beta = \beta_1 - \beta_2 \approx 1.0$) at $F_{100} = 6.97(\pm 0.13) \times 10^{-8}$ ph cm^{-2} s^{-1}. At fluxes brighter than the break flux, the source count distribution is consistent with Euclidean ($\beta_1 = 2.5$) while it is not at fainter fluxes. As Tab. 3 shows, these results do not change if the sample under study is enlarged to $|b| \geq 15°$.

6.2. A Global Fit

Because of the spectral selection effect discussed in § 3.1, the sky coverage derived in § 4.2 can be used only with samples which have a distribution of the photon indices similar to

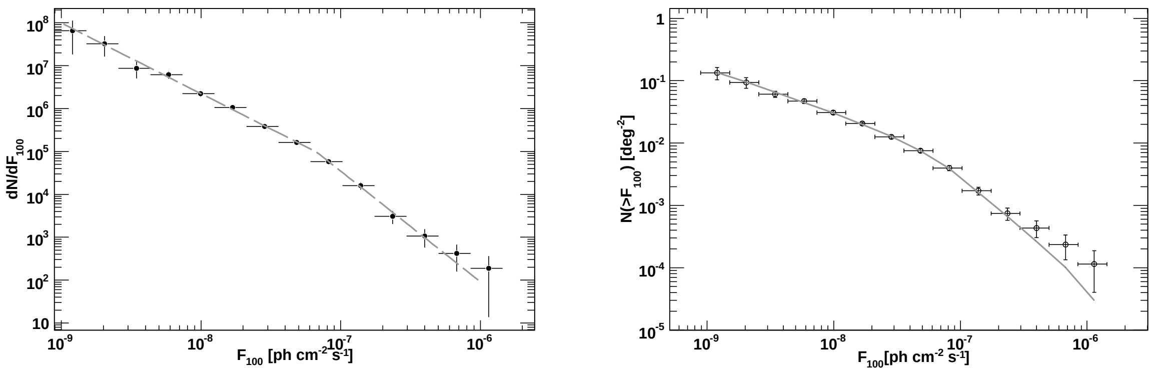

Fig. 9.— Differential (left) and cumulative (right) log N–log S for all sources with TS$\geq$ 50 and $|b| \geq 20°$. The dashed line is the best-fit broken power law model as reported in the text.

the one used in the simulations (i.e. a Gaussian with mean and dispersion of 2.40 and 0.28). Here we aim at overcoming this limitation by implementing for the first time a novel, more formal, analysis to derive the source count distribution. We aim at describing the properties of the sample in terms of a distribution function of the following kind:

$$\frac{dN}{dSd\Gamma} = f(S) \cdot g(\Gamma) \tag{5}$$

where $f(S)$ is the intrinsic flux distribution of sources and $g(\Gamma)$ is the intrinsic distribution of the photon indices. In this analysis, $f(S)$ is modeled as a double power-law function as in Eq. 4. The index distribution $g(\Gamma)$ is modeled a Gaussian function:

$$g(\Gamma) = e^{-\frac{(\Gamma-\mu)^2}{2\sigma^2}} \tag{6}$$

where μ and σ are respectively the mean and the dispersion of the Gaussian distribution. As it is clear from Eq. 5, we made the hypothesis that the $dN/dSd\Gamma$ function is factorizable in two separate distributions in flux and photon index. This is the most simple assumption that could be made and as it will be shown in the next sections it provides a good description of the data. Moreover, we emphasize, as already did in § 4, that this analysis implicitly assumes that the photon index distribution does not change with flux. This will be discussed in more details in the next sections.

This function is then fitted to all datapoints using a Maximum Likelihood approach as described in Sec. 3.2 of Ajello et al. (2009). In this method, the Likelihood function can be defined as:

$$L = \exp(-\mathrm{N}_{\mathrm{exp}}) \prod_{i=1}^{N_{\mathrm{obs}}} \lambda(S_i, \Gamma_i) \quad (7)$$

with $\lambda(S, \Gamma)$ defined as:

$$\lambda(S, \Gamma) = \frac{dN}{dSd\Gamma} \Omega(S, \Gamma) \quad (8)$$

where $\Omega(S, \Gamma)$ is the photon index dependent sky coverage and N_{obs} is the number of observed sources. This is generated from the same Monte Carlo simulation of § 4 with the difference that this time the detection probability is computed for each bin of the photon-index–flux plane as the ratio between detected and simulated sources (in that bin). This produces a sky coverage which is function of both the source flux and photon index.

The *expected* number of sources N_{exp} can be computed as:

$$N_{exp} = \int d\Gamma \int dS \lambda(S, \Gamma) \quad (9)$$

The maximum likelihood parameters are obtained by minimizing the function $C(= -2\ln L)$:

$$C = -2 \sum_{i}^{N_{obs}} \ln(\lambda(S_i, \Gamma_i)) - 2N \ \ln(\mathrm{N}_{\mathrm{exp}}) \quad (10)$$

while their associated $1\,\sigma$ errors are computed by varying the parameter of interest, while the others are allowed to float, until an increment of ΔC=1 is achieved. This gives an estimate of the 68 % confidence region for the parameter of interest (Avni 1976).

Once the $dN/dSd\Gamma$ has been determined, the standard differential source count distribution can be readily derived as:

$$\frac{dN}{dS} = \int_{-\infty}^{\infty} d\Gamma \frac{dN}{dSd\Gamma} \quad (11)$$

6.3. The Total Sample of Point Sources

The results of the best-fit model for the entire sample of sources (for TS≥50 and $|b| \geq 20°$) are reported in Tab. 4. Fig. 10 shows how well the best-fit model reproduces the observed index and flux distributions. The χ^2 test yields that the probabilities that the real distribution and the model line come from the same parent population are 0.98 and 0.97 for the photon index and flux distributions, respectively. In Fig. 11 the source count distribution obtained here is compared to the one derived using the standard approach of § 6.1; the good agreement is apparent.

We also derived the source count distributions of all objects which are classified as blazars (or candidate blazars) in our sample. This includes 352 out of the 425 objects reported in Tab. 2. The number of sources that lack association is 56 and thus the incompleteness of the blazar sample is $56/425 \approx 13\,\%$. A reasonable and simple assumption is that the 56 unassociated sources are distributed among the different source classes in a similar way as the associated portion of the sample (see Tab. 2). This means that 46 out of the 56 unassociated sources are likely to be blazars. As it is possible to notice both from the best-fit parameters of Tab. 4 and from Fig. 12, there is very little difference between the source count distributions of the entire sample and the one of blazars. This confirms on a statistical basis that most of the 56 sources without association are likely to be blazars. It is also clear from Fig. 10, that the model (e.g. Eq. 5) represents a satisfactory description of the data. This also implies that the *intrinsic* photon index distribution of blazars is compatible with a Gaussian distribution that does not change (at least dramatically) with source flux in the range of fluxes spanned by this analysis. A change in the average spectral properties of blazars with flux (and/or redshift) might be caused by the different cosmological evolutions of FSRQs and BL Lacs or by the spectral evolution of the two source classes with redshift. While it is something reasonable to expect, this effect is in the current dataset not observed. The luminosity function, which is left to a future paper, will allow us to investigate this effect in great detail.

6.4. FSRQs

For the classification of blazars as flat spectrum radio quasars (FSRQs) or BL Lacertae objects (BL Lacs) we use the same criteria adopted in Abdo et al. (2009a). This classification relies on the conventional definition of BL Lac objects outlined in Stocke et al. (1991), Urry & Padovani (1995), and Marcha et al. (1996) in which the equivalent width of the strongest optical emission line is $<5\,$Å and the optical spectrum shows a Ca II H/K break ratio $C<0.4$.

It is important to determine correctly the incompleteness of the sample when dealing with a sub-class of objects. Indeed, in the sample of Tab.2, 56 objects have no associations and 28 have either an uncertain or a tentative association with blazars. Thus the total

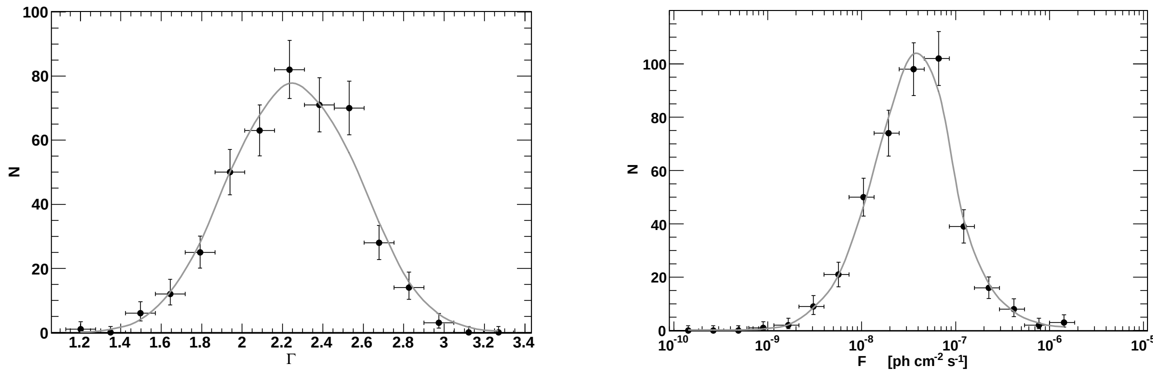

Fig. 10.— Distribution of photon indices (left) and fluxes (right) for the TS≥50 and $|b|$ ≥20° sources. The dashed line is the best fit $dN/dSd\Gamma$ model. Using the χ^2 test the probabilities that the data and the model line come from the same parent population are 0.98 and 0.97 for the photon index and flux distribution respectively.

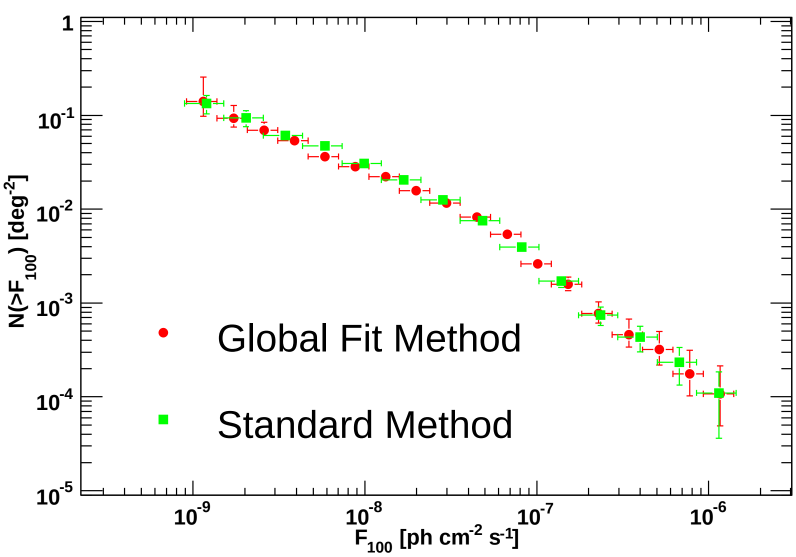

Fig. 11.— Comparison of log N–log S of the whole sample of (TS≥50 and $|b|$ ≥20°) sources built with the standard method (green datapoints, see § 6.1) and the global fit method (red datapoints,see § 6.2).

incompleteness is $84/425 = \sim$19 % when we refer to either FSRQs or BL Lac objects separately. The incompleteness levels of all the samples used here are for clarity reported also

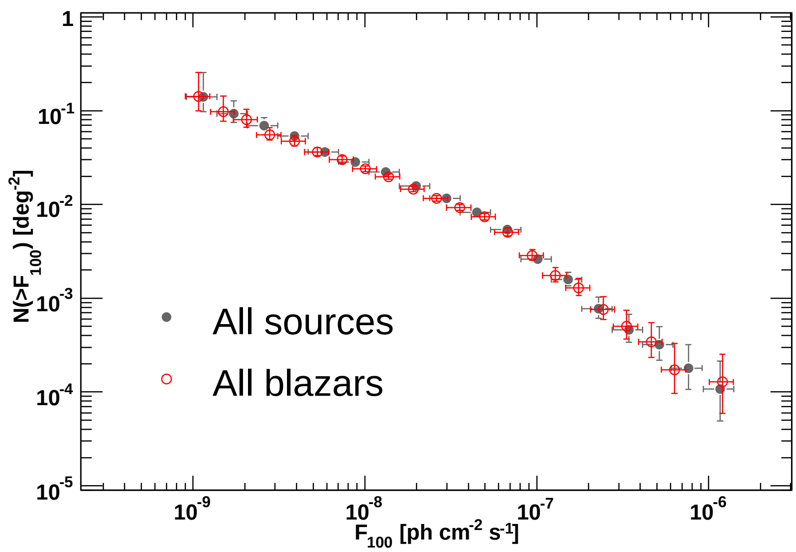

Fig. 12.— Comparison between log N–log S distributions of the whole sample of sources (solid circles) and blazars (open circles). The solid line are the respective best-fit models as reported in Tab. 4.

in Tab. 4. Since we did not perform dedicated simulations for the FSRQ and the BL Lac classes, their source count distributions can be derived only with the method described in § 6.2.

The best fit to the source counts (reported in Tab. 4) is a double power-law model with a bright-end slope of 2.41±0.16 and faint-end slope 0.70±0.30. The log N–log S relationship shows a break around $F_{100} = 6.12(\pm 1.30) \times 10^{-8}$ ph cm^{-2} s^{-1}. The intrinsic distribution of the photon indices of FSRQs is found to be compatible with a Gaussian distribution with mean and dispersion of 2.48±0.02 and 0.18±0.01 in agreement with what found previously in Tab. 1. The faint-end slope is noticeably flatter and this might be due to the fact that many of the unassociated sources below the break might be FSRQs. Fig. 13 shows how the best-fit model reproduces the observed photon index and flux distributions. The χ^2 test indicates that the probability that the real distribution and the model line come from the same parent population is $\geq$ 0.99 for both the photon index and flux distributions respectively. The left panel shows that the photon index distribution is not reproduced perfectly. This might be due to incompleteness or by the fact that the intrinsic distribution of photon indices is actually not Gaussian. However, a Kolmogorov-Smirnov (KS) test between the predicted and the observed distribution yields that both distributions have a probability of $\sim$ 96 % of being drawn from the same parent population. Thus the current dataset is compatible with the hypothesis that the intrinsic index distribution is Gaussian. The log N–log S of FSRQs is shown in Fig. 14.

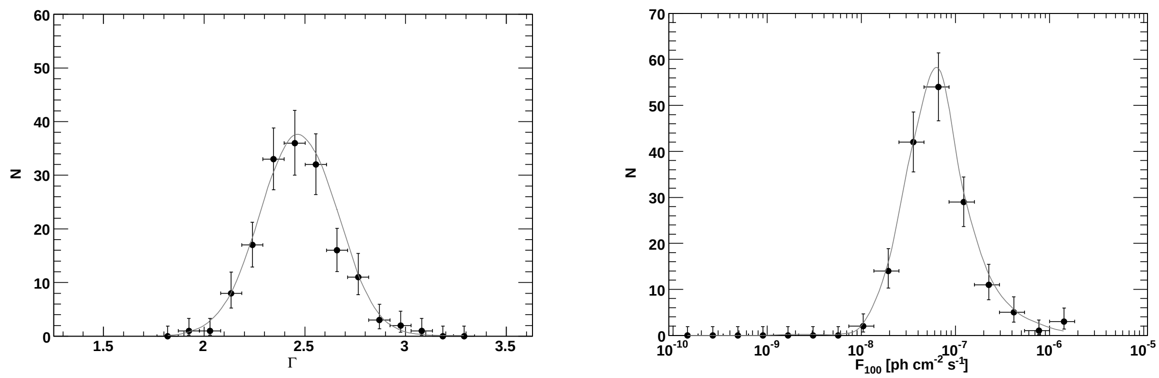

Fig. 13.— Distribution of photon indices (left) and fluxes (right) for the TS≥50 and $|b| \geq 20°$ sources associated with FSRQs.

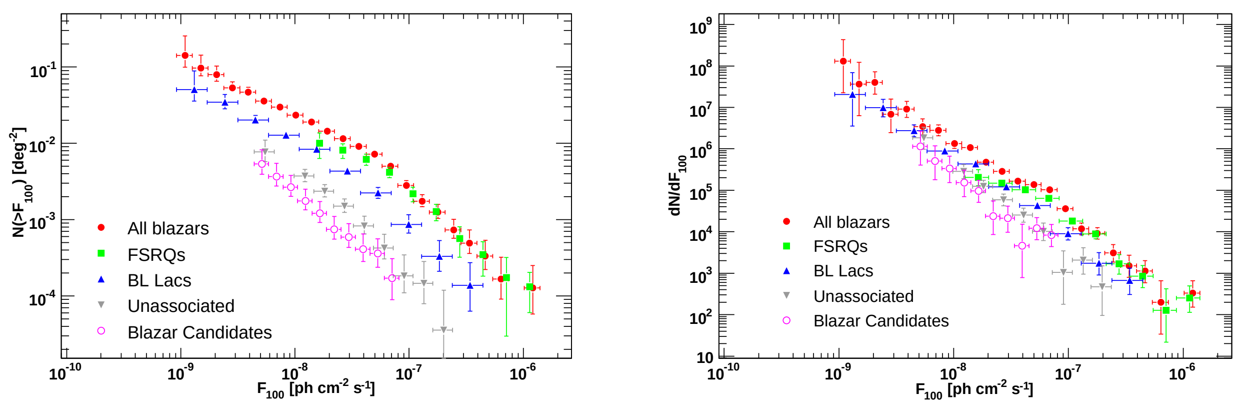

Fig. 14.— Cumulative (left) and differential (right) source count distribution of *Fermi* blazars and the sub-samples reported in Tab. 4. Given the selection effect towards spectrally hard sources, BL Lac objects are detected to fluxes fainter than FSRQs. The flattening at low fluxes of the FSRQs log$N$–log$S$ is probably due to incompleteness (see text for details). The “All Blazars” class also includes all those sources which are classified as blazar candidates (see Tab. 2 for details).

6.5. BL Lacs

The best-fit model of the source count distribution of the 161 BL Lac objects is again a broken power-law model. The break is found to be at F_{100} =6.77±1.30 × 10^{-8} ph cm^{-2} s^{-1} while the slopes below and above the break are 1.72±0.14 and 2.74±0.30 respectively. The intrinsic photon index distribution is found to be compatible with a Gaussian distribution with mean and dispersion of 2.18±0.02 and 0.23±0.01 respectively. These results are in good agreement with the one reported in Tab. 1. The best-fit parameters to the source counts distribution are reported in Tab. 4. Fig. 15 shows how the best-fit model reproduces the observed photon index and flux distributions. The χ^2 test indicates that the probability that the real distribution and the model line come from the same parent population is $\geq$ 0.99 for both the photon index and flux distributions respectively. The log N–log S of BL Lacs, compared to the one of FSRQs and blazars, is shown in Fig. 14.

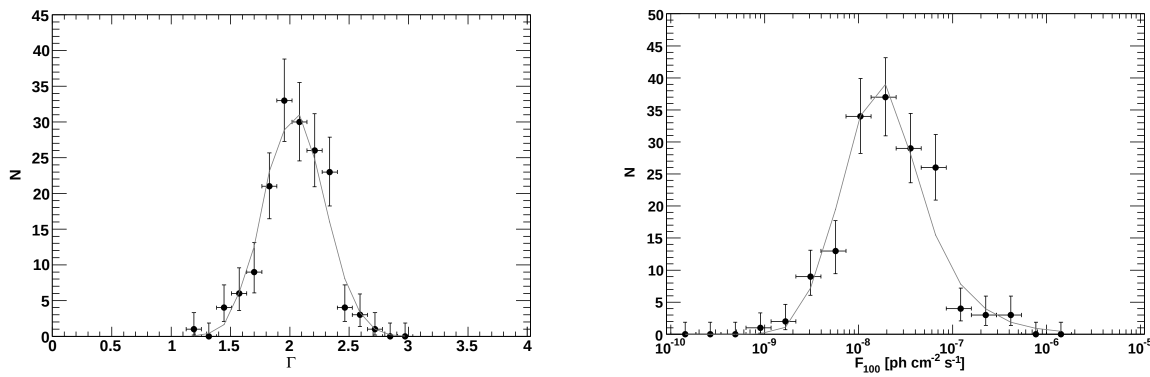

Fig. 15.— Distribution of photon indices (left) and fluxes (right) for the TS≥50 and $|b| \geq 20°$ sources associated with BL Lacs. The dashed line is the best fit $dN/dSd\Gamma$ model.

6.6. Unassociated Sources

We also constructed the log N–log S of the 56 sources which are unassociated and it is reported in Fig. 14. Their source count distribution displays a very steep bright-end slope (β_1=3.16±0.50), a break around ∼4.5×10^{-8} ph cm^{-2} s^{-1} and faint-end slope of 1.63±0.24. The intrinsic photon index distribution is found to be compatible with a Gaussian distribution with mean and dispersion of 2.29±0.03 and 0.20±0.01 respectively (see Tab. 4 for details). The extremely steep bright-end slope is caused by the fact that most (but not all) of the brightest sources have an association. Below the break the log N–log S behaves like the one of blazars with the difference that the index distribution is suggesting that probably most of the sources are BL Lac objects. Indeed as can be seen in Fig. 14 all the sources with $F_{100} \leq 4 \times 10^{-8}$ ph cm^{-2} s^{-1} are identified as BL Lac objects in our sample.

6.7. Unfolding Analysis

Finally we employ a different approach to evaluate the log N–log S distribution based on a deconvolution (unfolding) technique. This method allows reconstructing the distribution of the number of sources from the data without assuming any model, also taking into account the finite resolution (i.e. dispersion) of the sky coverage.

The purpose of the unfolding is to estimate the true distribution (cause) given the observed one (effect), and assuming some knowledge about the eventual migration effects (smearing matrix) as well as the efficiencies. The elements of the smearing matrix represent the probabilities to observe a given effect that falls in an observed bin $Effect_j$ from a cause in a given true bin $Cause_i$. In our case the observed distribution represents the number of sources as function of the observed flux above 100 MeV, while the true distribution represents the number of true sources as function of the true flux above 100 MeV. The unfolding algorithm adopted here is based on the Bayes theorem D'Agostini (1995).

The smearing matrix is evaluated using the Monte Carlo simulation described in the § 4. Its elements, $P(F100_{j,obs}|F100_{i,true})$, represent the probabilities that a source with a true flux above 100 MeV, $F100_{i,true}$, is reconstructed with an observed flux above 100 MeV, $F100_{j,obs}$. The data are assumed to be binned in histograms. The bin widths and the number of bins can be chosen independently for the distribution of the observed and reconstructed variables.

The log N–log S reconstructed with this method is shown in Fig. 16 and it is apparent that the source counts distributions derived with the 3 different methods are all in good agreement with each other.

6.8. Comparison with Previous Estimates

Fig. 16 shows that the log N–log S distributions displays a strong break at fluxes $F_{100} \approx 6 \times 10^{-8}$ ph cm^{-2} s^{-1}. This represents the first time that such a flattening is seen in the log N–log S of γ-ray sources, blazar in particular. This is due to the fact that *Fermi* couples a good sensitivity to the all-sky coverage thus allowing to determine the source counts distribution over more than 3 decades in flux.

Above fluxes of $F_{100} = 10^{-9}$ ph cm^{-2} s^{-1}, the surface density of sources is $0.12^{+0.03}_{-0.02}$ deg^{-2}. At these faint fluxes our comparison can only be done with predictions from different models. Dermer (2007) and Inoue & Totani (2009) predict a blazar surface density of respectively 0.030 deg^{-2} and 0.033 deg^{-2}. Both these predictions are a factor ~ 4 below the LAT measurement. However, it should be stressed that these models are based on the EGRET blazar sample which, because of strong selection effects against high-energy photons, counted a very limited number of BL Lac objects.

At brighter fluxes ($F_{100} \geq 5 \times 10^{-8}$ ph cm^{-2} s^{-1}) Dermer (2007) predicts a density of FSRQs and BL Lacs of $4.1{\times}10^{-3}$ deg^{-2} and $1.1{\times}10^{-3}$ deg^{-2} respectively. At the same flux, Mücke & Pohl (2000) predict a density of $1.21{\times}10^{-3}$ deg^{-2} and $3.04{\times}10^{-4}$ deg^{-2} respectively for FSRQs and BL Lac objects. The densities measured by *Fermi* are significantly larger, being $6.0(\pm 0.6) \times 10^{-3}$ deg^{-2} for FSRQs and $2.0(\pm 0.3) \times 10^{-3}$ deg^{-2} for BL Lacs.

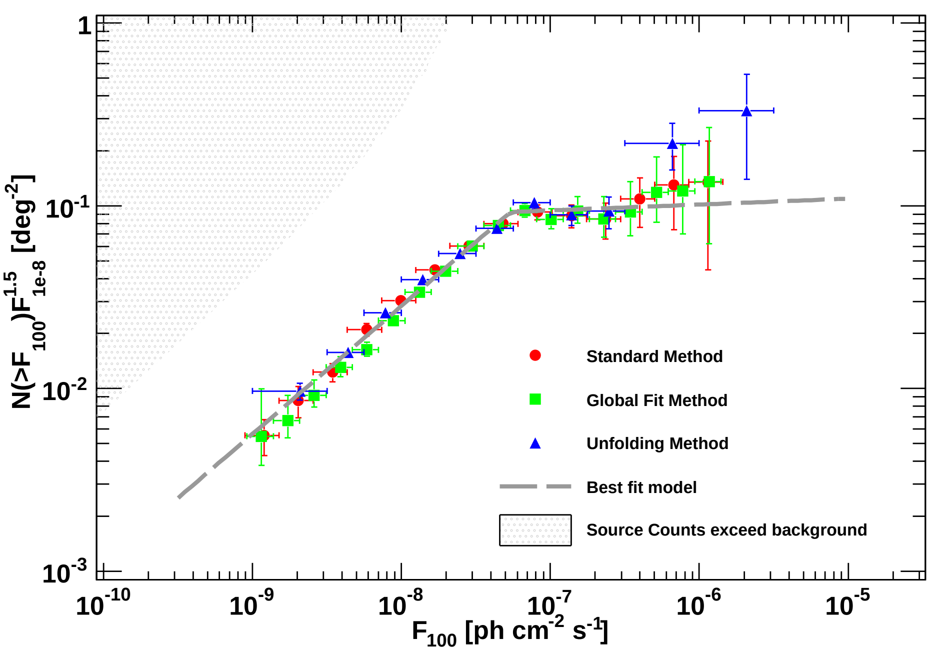

Fig. 16.— Source count distribution of *Fermi* point-like sources derived with three different methods. The distribution has been multiplied by $(F_{100}/10^{-8})^{1.5}$. The dashed line is the best fit model described in the text. The grey region indicates the flux at which a power law connecting the log N–log S break (at $\sim 6.6 \times 10^{-8}$ ph cm^{-2} s^{-1}) and that given flux exceeds the EGB emission (see text for details).

7. Analysis in the Different Energy Bands

The aim of the following analysis is to determine the contribution of point sources to the EGB in different contiguous energy bands. This is done by creating a log$N$–log$S$ distribution in 3 different energy bands: 0.1–1.0 GeV, 1.0–10.0 GeV and 10.0–100 GeV bands. This will allow us to study the spectrum of the unresolved emission from point sources and at the same time explore the properties of the source population in different bands. With this approach, the systematic uncertainty related to the flux estimate, given by the complex spectra of blazars (see \$ 5.3), will be removed. In addition, use of these bands should allow us to extend the survey region to $|b| \geq 10^{\circ}$ (see § 5.1).

The analysis follows the method outlined in § 4 with the difference that the final ML fit is restricted to the band under investigation. In the spectral fit, all parameters (including the photon index) are left free and are optimized by maximizing the likelihood function. Only sources that a given band have TS≥25 are considered detected in that band. Formally each band and related sample is treated as independent here and no prior knowledge of the source spectral behaviour is assumed. In the three bands, the samples comprise respectively 362, 597 and 200 sources detected for $|b| \geq 10^{\circ}$ and TS≥ 25.

In both the soft and the medium band (i.e. 0.1–1.0 GeV and 1.0–10.0 GeV), the log$N$–log$S$ is well described by a double power-law model, while in the hardest band (10–100 GeV) the log$N$–log$S$ is compatible with a single power-law model with a differential slope of 2.36±0.07. The results of the best-fit models are reported in Tab. 5 and are shown in Fig. 17. The *spectral bias* (see § 2) is the strongest in the soft band while it is absent in the high-energy band, being already almost negligible above 1 GeV.

From the log$N$–log$S$ in the whole band we would expect (assuming a power law with a photon index of 2.4 and that the blazar population is not changing dramatically with energy) to find breaks at: 6.7×10^{-8}, 2.6×10^{-9}, and 1×10^{-10} ph cm^{-2} s^{-1} for the soft, medium, and hard bands respectively. Indeed these expectations are confirmed by the ML fits in the individual bands (e.g. see Tab. 5). The hard band constitutes the only exception where the flux distribution barely extends below the flux at which the break might be observed.

The average spectral properties of the sample change with energy. We find that the *intrinsic* index distribution is compatible with a Gaussian distribution with means of 2.25±0.02, 2.43±0.03, and 2.17±0.05. In the three bands the fraction of BL Lac-to-FSRQ is: 0.61, 1.14, and 3.53 respectively with identification incompletenesses of 0.18, 0.25, and 0.25 respectively. It is apparent that the hardest band is the best one for studying BL Lac objects since the contamination due to FSRQs is rather small.

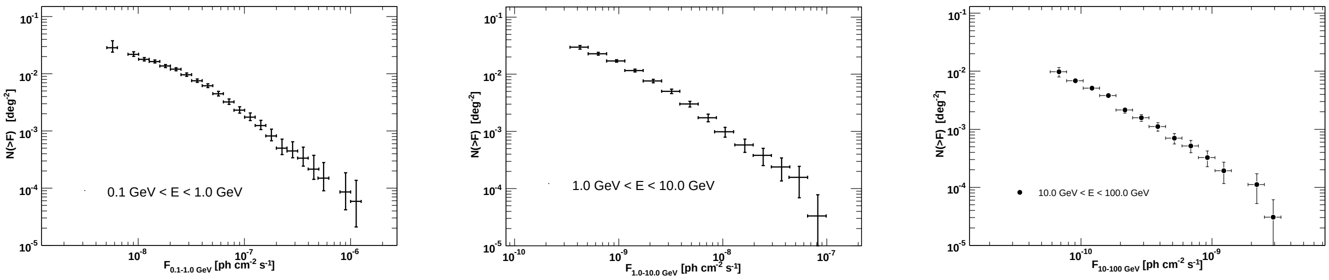

Fig. 17.— Source count distributions for the soft (0.1-1.0 GeV, left), medium (1.0–10.0 GeV, center) and high energy (10.0–100.0 GeV, right) band reconstructed with the method reported in § 6.2.

8. Contribution of Sources to the Diffuse Background

The source count distribution can be used to estimate the contribution of point-like sources to the EGB emission. This allows us to determine the fraction of the GeV diffuse emission that arises from point-like source populations measured by *Fermi*. As specified in § 2, this estimate does not include the contribution of sources which have been directly detected by *Fermi* since these are not considered in the measurement of the diffuse background. This estimate includes all those sources which, because the detection efficiency changes with flux, photon index and position in the sky, have not been detected.

The diffuse emission arising from a class of sources can be determined as:

$$F_{\rm diffuse} = \int_{S_{\rm min}}^{S_{\rm max}} dS \int_{\Gamma_{\rm min}}^{\Gamma_{\rm max}} d\Gamma \frac{dN}{dSd\Gamma} S \left(1 - \frac{\Omega(\Gamma, S)}{\Omega_{\rm max}}\right) \tag{12}$$

where $\Omega_{\rm max}$ is the geometrical sky area and the $(1 - \Omega(\Gamma, S)/\Omega_{\rm max})$ term takes into account that the threshold at which LAT detects sources depends on both the photon index and the source flux. We note that neglecting the dependence of Ω on the photon index (i.e. using the mono-dimensional sky coverage reported in Fig. 7) would result in an underestimate of the diffuse flux resolved by *Fermi* into point-sources. The limits of integration of Eq. 12 are $\Gamma_{\rm min} = 1.0$, $\Gamma_{\rm max} = 3.5$, and $S_{\rm max} = 10^{-3}$ ph cm^{-2} s^{-1}. We also note that the integrand of Eq. 12 goes to zero for bright fluxes or for photon indices which are either very small or very large; thus the integration is almost independent of the parameters reported above. The integration is not independent of the value of $S_{\rm min}$ which is set to the flux of the faintest source detected in the sample. For the analysis of the whole band $S_{\rm min}$=9.36×10^{-10} ph cm^{-2} s^{-1} while for the low, medium and hard band $S_{\rm min}$ is set to: 5.17×10^{-9} ph cm^{-2} s^{-1}, 3.58×10^{-10} ph cm^{-2} s^{-1}, and 6.11×10^{-11} ph cm^{-2} s^{-1} respectively.

Since in the measurement of Abdo et al. (2010d) the sources which are subtracted are those detected in 9 months of operation, the coverage used in Eq. 12 is the one corresponding to the 9 months survey. The uncertainties on the diffuse flux have been computed by performing a bootstrap analysis. Integrating Eq. 12 we find that the point source contribution is $1.63(\pm0.18)\times10^{-6}$ ph cm^{-2} s^{-1} sr^{-1} where the systematic uncertainty is 0.6×10^{-6} ph cm^{-2} s^{-1} sr^{-1}. This corresponds to $16(\pm1.8)$ % (±7 % systematic uncertainty) of the Isotropic diffuse emission measured by LAT (Abdo et al. 2010d) above 100 MeV. This small fraction is a natural consequence of the break of the source counts distribution. However, it is also possible to show that the parameter space for the faint-end slope β_2 is rather limited and that a break must exist in the range of fluxes spanned by this analysis. Indeed, for a given β_2 (and all the other parameters of the log N–log S fixed at their best-fit values) one can solve Eq. 12 to determine the flux at which the integrated emission of point sources exceeds the one of the EGB. Repeating this exercise for many different values of the β_2 parameter yields an exclusion region which constrains the behavior of the log N–log S at low fluxes. The results of this exercise are shown in Fig. 16. From this Figure it is apparent that the log N–log S *must* break between $F_{100}\approx2\times10^{-9}$ ph cm^2 s^{-1} and $F_{100}\approx6.6\times10^{-8}$ ph cm^2 s^{-1}. For a small break (e.g. $\beta_1-\beta_2\approx0.2-0.3$ and then $\beta_2\approx$2.2–2.3), the integrated emission of point sources would still match the intensity of the diffuse background at $F_{100}\approx10^{-9}$ ph cm^2 s^{-1} which are sampled by *Fermi*. Thus not only the break has to exist, but this simple analysis shows that it has to be strong (see also § 8.3), not to exceed the intensity of the diffuse emission.

The log$N$–log$S$ in the whole band goes deeper than the source count distributions derived in the smaller bands. This is clearly shown in Fig. 18. Given the fact that most of the source flux is emitted below 1 GeV (for reasonable photon indices), the source count distribution in the soft band (0.1–1.0 GeV) is the one which gets closer to the log$N$–log$S$ in the whole band in terms of resolved diffuse flux.

The log N–log S in the whole bands shows a strong break with a faint-end slope (e.g. β_2) robustly constrained to be $<$2. In this case the integral reported in Eq. 12 converges for small fluxes and it can be evaluated at zero flux to assess the maximum contribution of *Fermi*-like sources to the diffuse background. This turns out to be $2.39(\pm0.48)\times10^{-6}$ ph cm^{-2} s^{-1} sr^{-1} (1.26×10^{-6} ph cm^{-2} s^{-1} sr^{-1} systematic uncertainty) which represents $23(\pm5)$ % (12 % systematic uncertainty) of the *Fermi* diffuse background (Abdo et al. 2010d). This is a correct result as long as the log N–log S of point-sources (i.e. blazars) does not become steeper at fluxes below the ones currently sampled by *Fermi*. A given source population normally exhibits a source count distribution with a single downwards break (e.g. see the case of radio-quiet AGN in Cappelluti et al. 2007). This break is of cosmological origin since it coincides with the change of sign of the evolution of that population. As can be clearly seen in the redshift distribution in Abdo et al. (2010e) the epoch of maximum growth of blazars corresponds to redshift 1.5–2.0 which coincides well with the peak of the star formation in the Universe (e.g. Hopkins & Beacom 2006). Since *Fermi* is already sampling this population it is reasonable to expect no other breaks in the source count distribution of blazars. Under this assumption, the result of the integration of Eq. 12 are correct. The results of this exercise are shown in Fig. 19 and summarized in Tab. 6. Since the 10–100 GeV source counts distribution does not show a break, its integral diverges for small fluxes. Thus, in both Fig. 19 and Tab. 6 we decided to adopt, as a lower limit to the contribution of sources to the diffuse emission in this band, the value of the integral evaluated at the flux of the faintest detected source.

The different levels of contribution to the diffuse background as a function of energy band might be the effect of the mixing of the two blazar populations. In other words, as shown in § 7, FSRQs are the dominant population below 1 GeV while BL Lacs are the dominant one above 10 GeV. Given also that FSRQs are softer than BL Lacs (see also § 3), it is naturally to expect a modulation in the blazar contribution to the diffuse emission as a function of energy. This can clearly be seen in Fig. 20 which shows the contribution of FSRQs and BL Lacs to the diffuse emission. This has been computed integrating the source count distribution of Tab. 4 to the minimum detected source flux which is 9.36×10^{-10} ph cm^{-2} s^{-1} and and 1.11×10^{-8} ph cm^{-2} s^{-1} for BL Lacs and FSRQs respectively. It is clear that FSRQs are contributing most of the blazar diffuse emission below 1 GeV while BL Lacs, given their hard spectra, dominate above a few GeVs. The spectrum of the diffuse emission arising from the blazar class is thus curved, being soft at low energy (e.g. below 1 GeV) and hard at high energy (above 10 GeV), in agreement with the results of the analysis of the source count distributions in different bands.

8.1. Additional Tests

8.2. Source Count Distribution above 300 MeV

The effective area of the LAT decreases quickly below 300 MeV while at the same time both the PSF size and the intensity of the diffuse background increase (e.g. see Atwood et al. 2009). In particular at the lowest energies, systematic uncertainties in the instrument response might compromise the result of the maximum likelihood fit to a given source (or set of sources). In order to overcome this limitation we constructed, with the method outlined in § 7, the log N–log S of point sources in the 300 MeV–100 GeV band. Considering that in the E> 100 MeV band the log N–log S shows a break around 6-7$\times10^{-8}$ ph cm^{-2} s^{-1} and assuming a power law with a photon index of 2.4, we would expect to detect a break in the (E$\geq$300 MeV) log N–log S around $\sim1.5\times10^{-8}$ ph cm^{-2} s^{-1}. Indeed, as shown in Fig. 21, the

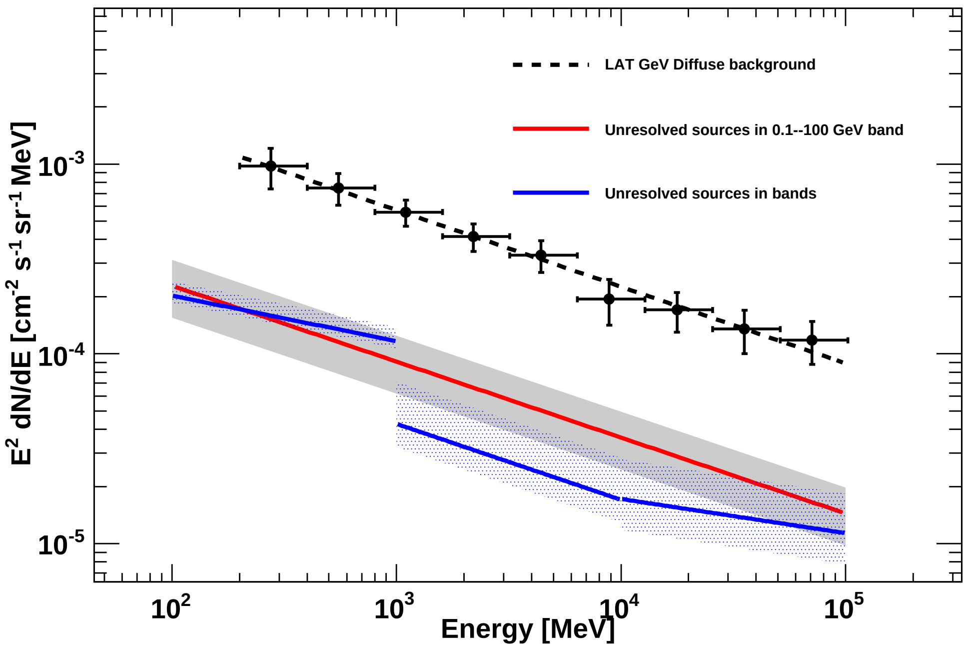

Fig. 18.— Contribution of point-sources to the diffuse GeV background. The red solid line was derived from the study of the log$N$–log$S$ in the whole band while the blue solid lines come from the study of individual energy bands (see § 7). The bands (grey solid and hatched blue) show the total (statistical plus systematic) uncertainty.

break is detected at $1.68(\pm0.33)\times10^{-8}$ ph cm^{-2} s^{-1}. Moreover, as Fig. 21 shows, the break of the log N–log S and the one of the sky coverage are at different fluxes. More precisely, the source counts start to bend down before the sky coverage does it. This is an additional confirmation, along with the results of § 7, that the break of the log N–log S is not caused by the sky coverage. The parameters of this additional source count distribution are reported for reference in Tab. 5.

8.3. Simulating a log N–log S without a break

In order to rule out the hypothesis that the sources detected by *Fermi* produce most of the GeV diffuse emission, we performed an additional simulation. In this exercise the input log N–log S is compatible with a single power law with a differential slope of 2.23. At bright fluxes this log N–log S is compatible with the one reported in Abdo et al. (2009a)

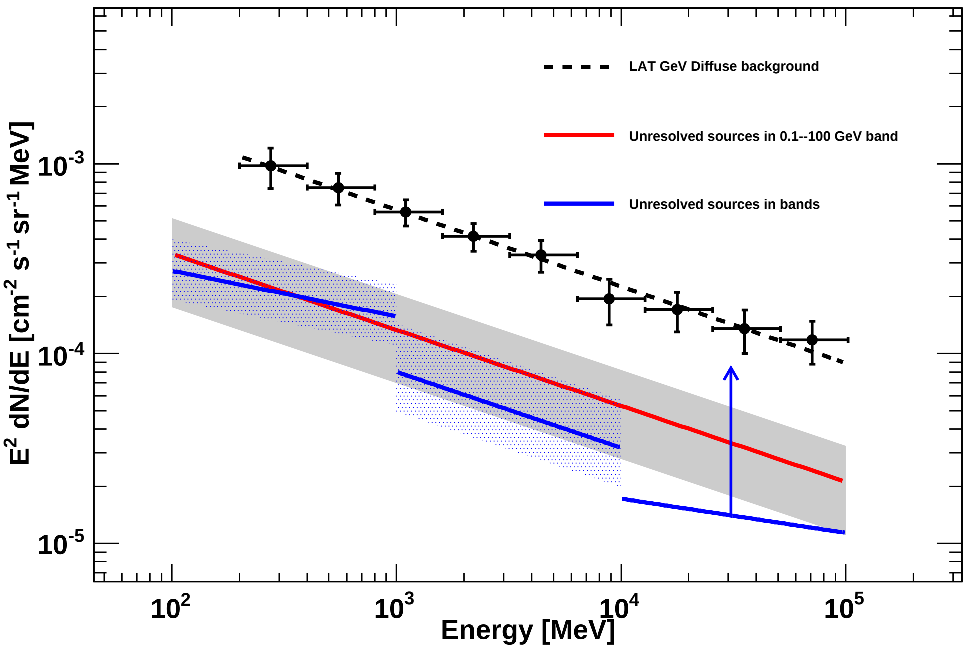

Fig. 19.— Contribution of point-sources to the diffuse GeV background obtained by extrapolating and integrating the log N–log S to zero flux. The red solid line was derived from the study of the log$N$–log$S$ in the whole band while the blue solid lines come from the study of individual energy bands (see § 7). The bands (grey solid and hatched blue) show the total (statistical plus systematic) uncertainty. The arrow indicates the lower limit on the integration of Eq. 12 for the 10–100 GeV band.

and at fluxes $F_{100} \geq 10^{-9}$ ph cm^{-2} s^{-1} accounts for $\sim$70 % of the EGB. In this scenario the surface density of sources at $F_{100} \geq 10^{-9}$ ph cm^{-2} s^{-1} is 0.8 deg^{-2} (while the one we derived in § 6.8 is 0.12 deg^{-2}). To this simulation we applied the same analysis steps used for both the real data and the simulations analyzed in § 4. Fig. 22 compares the flux distribution of the sources detected in this simulation with the distribution of the real sources detected by LAT and also with the sources detected in one of the simulations used in § 4. It is apparent that the flux distribution of the sources detected in the simulation under study here is very different from the other two.

Indeed, in the case point-like sources produce most of the EGB *Fermi* should detect many more medium-bright sources than are actually seen. A Kolmogorv-Smirnov test yields that the probability that the flux distribution (arising from the log N–log$S$ tested in this section) comes from the same parent population as the real data is $\leq 10^{-5}$. This probability

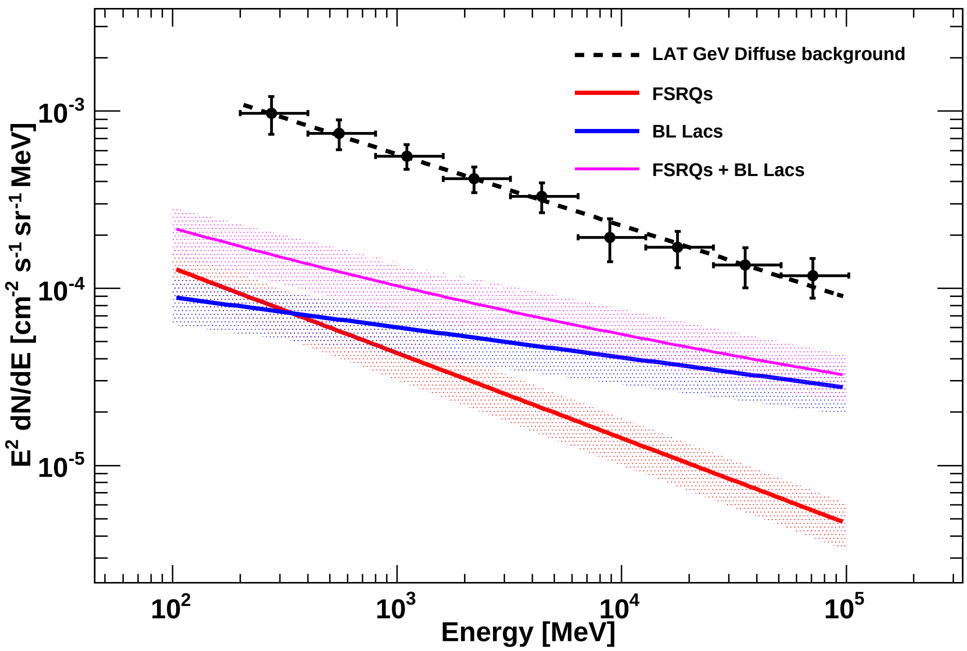

Fig. 20.— Contributions of different classes of blazars to the diffuse GeV background obtained by integrating the log N–log S. The red and the blues solid lines show the contribution of FSRQs and BL Lacs respectively, while the pink solid line shows the sum of the two. The bands around each line show the total (statistical plus systematic) uncertainty.

becomes 5×10^{-4} if the χ^2 test is used. The KS test between the flux distribution of one of the simulations used in § 4 and the real data yields a probability of ∼87 % that both come from the same parent population while it is ∼91 % if the χ^2 test is used.

Thus the hypothesis that *Fermi* is resolving (for $F_{100} \geq 10^{-9}$ ph cm^{-2} s^{-1}) the majority of the diffuse background can be ruled out at high confidence.

9. Discussion and Conclusions

Fermi provides a huge leap in sensitivity for the study of the γ-ray sky with respect its predecessor EGRET. This work focuses on the global intrinsic properties of the source population detected by *Fermi* at high Galactic latitudes.

We constructed the source count distribution of all sources detected above $|b| \geq 20°$.

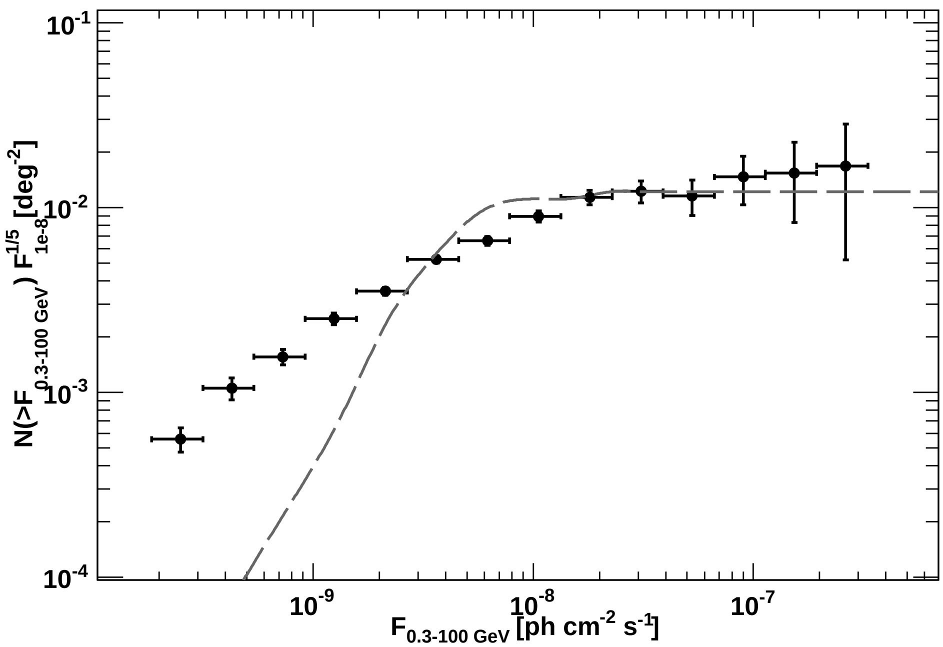

Fig. 21.— Source count distribution of all (TS$\geq$ 25, $|b| \geq 10°$) sources in the 300 MeV–100 GeV band. The distribution has been multiplied by $(F_{100}/10^{-8})^{1.5}$. The dashed line shows the sky coverage (scaled by an arbitrary factor) used to derive the source counts. Note that the break of the log N – log S and that one of the sky coverage are at different fluxes.

This distribution extends over three decades in flux and is compatible at bright fluxes (e.g. $F_{100} \geq 6\times10^{-8}$ ph cm^{-2} s^{-1}) with a Euclidean function. Several methods have been employed to show that at fainter fluxes the log N–log S displays a significant flattening. We believe that this flattening has a cosmological origin and is due to the fact that *Fermi* is already sampling, with good accuracy, the part of the luminosity function which shows negative evolution (i.e. a decrease of the space density of sources with increasing redshift). This is the first time that such flattening has been found in the source count distributions of γ-ray sources and blazars. We also showed that the log N–log S of blazars follows closely that of point source, showing that most of the unassociated high-latitude sources in the 1FLG catalog are likely to be blazars. At the fluxes currently sampled by *Fermi* (e.g. $F_{100} \geq 10^{-9}$ ph cm^{-2} s^{-1}) the surface density of blazars is $0.12^{+0.03}_{-0.02}$ deg^{-2} and this is found to be a factor $\sim$4 larger than previous estimates.

The average intrinsic spectrum of blazars is in remarkably good agreement with the

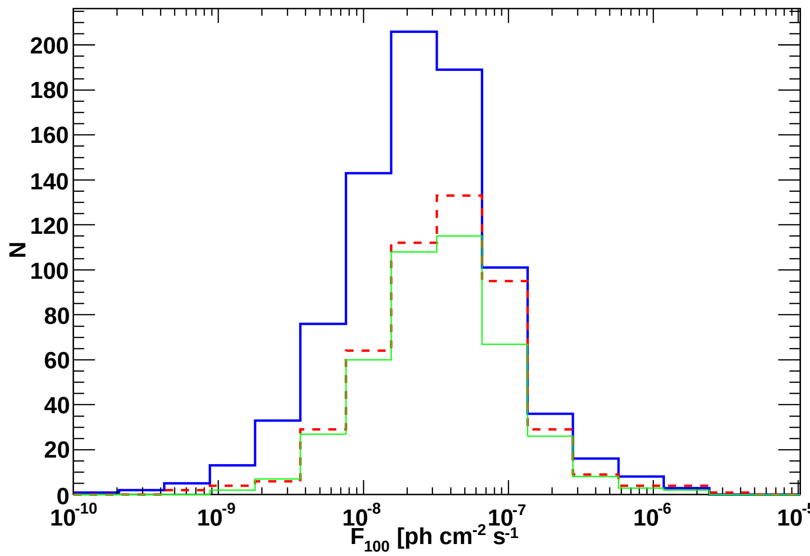

Fig. 22.— Flux distributions of detected sources (TS≥50 and $|b| \geq 20°$) for three different realizations of the γ-ray sky. The solid thick line corresponds to a log N – log S distribution which resolves approximately ∼70% of the GeV diffuse background, while the dashed line corresponds to the log N–log S derived in this work which resolves approximately ∼23 % of the diffuse background. For comparison the thin solid line shows the flux distributions of the real sample of sources detected by *Fermi*.

spectrum of the GeV diffuse emission recently measured by *Fermi* (Abdo et al. 2010d). Nevertheless, integrating the log N–log S, to the minimum detected source flux, shows that at least $16.0^{+2.4}_{-2.6}$ % (the systematic uncertainty is an additional 7 %) of the GeV background can be accounted for by source populations measured by *Fermi*. This is a small fraction of the total intensity and it is bound not to increase dramatically unless the log N–log$S$ becomes steeper at fluxes below 10^{-9} ph cm^{-2} s^{-1}. This generally never happens unless a different source class starts to be detected in large numbers at fainter fluxes.

Thompson et al. (2007) predict the integrated emission of starburst galaxies to be 10^{-6} ph cm^{-2} s^{-1} sr^{-1} (above 100 MeV). This would represent ∼10 % of the LAT diffuse background and would be comparable (although a bit less) to that of blazars found here. Indeed, their prediction that M82 and NGC 253 would be the first two starburst galaxies to be detected has been fulfilled (Abdo et al. 2010a). A similar contribution to the GeV diffuse background should arise from the integrated emission of normal star forming galaxies (Pavlidou & Fields 2002). In both cases (normal and starburst galaxies) γ-rays are produced from the interaction of cosmic rays with the interstellar gas (e.g. see Abdo et al. 2009b). It is natural to expect that both normal and starburst galaxies produce a fraction of the diffuse emission since now both classes are certified γ-ray sources (see e.g. Abdo et al. 2010b).

It is also interesting to note that pulsars represent the second largest population in our high-latitude sample (see Tab. 2). According to Faucher-Giguere & Loeb (2009) pulsars and in particular millisecond pulsars can produce a relevant fraction of the GeV diffuse emission. However, given the strong break, typically at a few GeVs, in their spectra (e.g. see Abdo et al. 2010f), millisecond pulsars are not expected to contribute much of the diffuse emission above a few GeVs. Finally radio-quiet AGN might also contribute to the GeV diffuse background. In these objects the γ-ray emission is supposedly produced by a non-thermal electrons present in the corona above the accretion disk (see e.g. Inoue et al. 2008, for details). Inoue & Totani (2009) predict that, at fluxes of $F_{100} \leq 10^{-10}$ ph cm^{-2} s^{-1}, radio-quiet AGN outnumber the blazars. According to their prediction, most of background could be explained in terms of AGN (radio-quiet and radio-loud).

It is thus clear that standard astrophysical scenarios can be invoked to explain the GeV extragalactic diffuse background. However, the main result of this analysis is that blazars account only for $<$40 % of it[4]. It remains a mystery why the average spectrum of blazars is so similar to the EGB spectrum. Taken by itself, this finding would lead to believe that blazars might account for the entire GeV diffuse background. However, we showed (see Fig. 22 and § 8.3 for details) that in this case *Fermi* should have detected a much larger number (up to $\sim$50 %) of medium-bright sources with a typical flux of $F_{100} \geq 10^{-8}$ ph cm^{-2} s^{-1}. This scenario can thus be excluded with confidence. Thus, the integrated emission from other source classes should still have a spectrum declining as a power-law with an index of ~ 2.4. This does not seem to be a difficult problem to overcome. Indeed, at least in the case of star forming galaxies we note that in the modeling of both Fields et al. (2010) and Makiya et al. (2010) the integrated emission from these sources displays a spectrum similar to the EGB one (at least for energies above 200 MeV). Moreover, in this work we also found that the contribution to the diffuse emission of FSRQs and BL Lacs is different, FSRQs being softer than BL Lacs. Thus, the summed spectrum of their integrated diffuse emission is curved, softer at low energy and hard at high ($>$ 10 GeV) energy. This makes it slightly different from the featureless power-law of the diffuse background. All the estimates presented here will be refined with the derivation of the blazar luminosity function which is left to a follow-up paper.

[4]This includes extrapolating the source counts distribution to zero flux and taking into account statistical and systematic uncertainties.

Table 3. Results of the power-law fits to the differential source count distributions obtained with the standard method of § 6.1

		Sample Limits		Best-fit Parameters			
SAMPLE	# Objects	TS≥	$\|b\| \geq$	A[a]	β_1	S_b[b]	β_2
ALL	425	50	20°	$1.15^{+0.15}_{-0.15}$	$2.63^{+0.22}_{-0.19}$	$6.97^{+1.28}_{-1.29}$	$1.64^{+0.06}_{-0.07}$
ALL	483	50	15°	$1.74^{+0.16}_{-0.16}$	$2.60^{+0.19}_{-0.17}$	$6.40^{+1.04}_{-1.08}$	$1.60^{+0.06}_{-0.07}$

[a]In units of 10^{-14} cm^2 s deg^{-2}.

[b]In units of 10^{-8} ph cm^{-2} s^{-1} (0.1≤E≤100 GeV).

Table 4. Results of the best fits to the source count distributions.

			Sample Limits		Best-fit Parameters					
SAMPLE	# Objects	Incompl.	TS≥	$\lvert b \rvert \geq$	A[a]	β_1	S_b[b]	β_2	μ	σ
ALL	425	0	50	20°	16.46±0.80	2.49±0.12	6.60±0.91	1.58±0.08	2.36±0.02	0.27±0.01
BLAZAR	352	0.13	50	20°	18.28±1.00	2.48±0.13	7.39±1.01	1.57±0.09	2.37±0.02	0.28±0.01
FSRQ	161	0.19	50	20°	72.41±5.76	2.41±0.16	6.12±1.30	0.70±0.30	2.48±0.02	0.18±0.01
BL Lac	163	0.19	50	20°	0.106±0.009	2.74±0.30	6.77±1.30	1.72±0.14	2.18±0.02	0.23±0.01
Unassociated	56	0	50	20°	$3.12(\pm 0.5) \times 10^{-5}$	3.16±0.50	4.48±1.3	1.63±0.24	2.29±0.03	0.20

[a]In units of 10^{-14} cm^2 s deg^{-2}.

[b]In units of 10^{-8} ph cm^{-2} s^{-1}.

Table 5. Results of the best fits to the source counts distributions in different Energy bands. Parameters without an error estimate were kept fixed during the fitting stage.

			Sample Limits		Best-fit Parameters					
BAND	# Objects	Incompl.	TS≥	$\lvert b \rvert \geq$	A[a]	β_1	S_b[b]	β_2	μ	σ
0.1–1.0 GeV	362	0	25	10°	4.00±0.21	$2.55^{+0.17}_{-0.22}$	$5.75^{+0.44}_{-2.22}$	$1.38^{+0.13}_{-0.46}$	$2.25^{+0.02}_{-0.02}$	$0.32^{+0.01}_{-0.01}$
1.0–10.0 GeV	597	0	25	10°	1.097±0.05	$2.38^{+0.15}_{-0.14}$	0.23±0.06	$1.52^{+0.8}_{-1.1}$	2.43	$0.40^{+0.02}_{-0.02}$
10.0–100.0 GeV	200	0	25	10°	$8.3(\pm0.6)\times10^{-3}$	$2.364^{+0.07}_{-0.07}$	...	...	2.17±0.05	$0.82^{+0.05}_{-0.05}$
0.3–100.0 GeV	759	0	25	10°	5.33±0.19	$2.44^{+0.15}_{-0.11}$	$1.69^{+0.33}_{-0.33}$	$1.70^{+0.06}_{-0.07}$	$2.35^{+0.02}_{-0.02}$	$0.30^{+0.01}_{-0.01}$

[a]In units of 10^{-14} cm^2 s deg^{-2}.

[b]In units of 10^{-8} ph cm^{-2} s^{-1}.

Table 6. Diffuse emission arising from point sources. The lower part of the table shows the values of the integrated emission when the source counts distributions are extrapolated to zero flux. Errors are statiscal only (see § 5 for a discussion about systematic uncertainties).

Band (GeV)	EGB Intensity[a] (ph cm^{-2} s^{-1} sr^{-1})	Point Source Diffuse Emission (ph cm^{-2} s^{-1} sr^{-1})	Fraction of EGB Intensity (%)	S_{min}[b] (ph cm^{-2} s^{-1})
0.1–100	1.03×10^{-5}	$1.63(\pm0.18)\times10^{-6}$	$15.8(\pm1.8)$	9.36
0.1–1.0	9.89×10^{-6}	$1.54^{+0.29}_{-0.13}\times10^{-6}$	$15.5^{+2.9}_{-1.3}$	51.1
1.0–10	3.85×10^{-7}	$2.93^{+1.95}_{-0.71}\times10^{-8}$	$7.6^{+5.0}_{-1.8}$	3.58
10–100	1.50×10^{-8}	$1.36^{+0.84}_{-0.43}\times10^{-9}$	$9.0^{+5.6}_{-2.8}$	0.61
0.1–100	1.03×10^{-5}	$2.39(\pm0.48)\times10^{-6}$	$22.5(\pm1.8)$	0
0.1–1.0	9.89×10^{-6}	$2.07^{+0.98}_{-0.61}\times10^{-6}$	$20.9^{+10.0}_{-6.1}$	0
1.0–10	3.85×10^{-7}	$5.49^{+4.36}_{-2.10}\times10^{-8}$	$14.2^{+11.2}_{-5.4}$	0
10–100	1.50×10^{-8}	$>1.36\times10^{-6}$	>9.0	0[c]

[a]The intentisities of the EGB emission are derived from Abdo et al. (2010d).

[b] Lower flux of integration of the source counts distributions (see Eq. 12) in units of 10^{-10} ph cm^{-2} s^{-1}.

[c]The source counts distribution in the 10–100 GeV does not show a break and thus, its integral to zero flux diverges. As a lower limit on the diffuse emission, we adopted the value computed at the faintest detected source.

Helpful comments from the referee are acknowledged. The *Fermi* LAT Collaboration acknowledges generous ongoing support from a number of agencies and institutes that have supported both the development and the operation of the LAT as well as scientific data analysis. These include the National Aeronautics and Space Administration and the Department of Energy in the United States, the Commissariat à l'Energie Atomique and the Centre National de la Recherche Scientifique / Institut National de Physique Nucléaire et de Physique des Particules in France, the Agenzia Spaziale Italiana and the Istituto Nazionale di Fisica Nucleare in Italy, the Ministry of Education, Culture, Sports, Science and Technology (MEXT), High Energy Accelerator Research Organization (KEK) and Japan Aerospace Exploration Agency (JAXA) in Japan, and the K. A. Wallenberg Foundation, the Swedish Research Council and the Swedish National Space Board in Sweden. Additional support for science analysis during the operations phase is gratefully acknowledged from the Istituto Nazionale di Astrofisica in Italy and the Centre National d'Études Spatiales in France.

Facilities: Fermi/LAT.

REFERENCES

Abdo, A. A., et al. 2009a, ApJ, 700, 597

—. 2009b, ApJ, 703, 1249

—. 2010a, ApJ, 709, L152

—. 2010b, ApJS, 188, 405

—. 2010c, ApJ, 710, 1271

—. 2010d, Physical Review Letters, 104, 101101

—. 2010e, ApJ, 715, 429

—. 2010f, ApJ, 713, 154

Ahn, E., Bertone, G., Merritt, D., & Zhang, P. 2007, Phys. Rev. D, 76, 023517

Ajello, M., Greiner, J., Kanbach, G., Rau, A., Strong, A. W., & Kennea, J. A. 2008, ApJ, 678, 102

Ajello, M., et al. 2009, ApJ, 699, 603

Atwood, W. B., et al. 2009, ApJ, 697, 1071

Avni, Y. 1976, ApJ, 210, 642

Bergström, L. 2000, Reports on Progress in Physics, 63, 793

Berrington, R. C., & Dermer, C. D. 2003, ApJ, 594, 709

Burnett, T. H., Kerr, M., & Roth, M. 2009, ArXiv:0912.3855

Cappelluti, N., et al. 2007, ApJS, 172, 341

Chiang, J., & Mukherjee, R. 1998, ApJ, 496, 752

Ciprini, S., et al. 2007, in American Institute of Physics Conference Series, Vol. 921, The First GLAST Symposium, ed. S. Ritz, P. Michelson, & C. A. Meegan, 546–547

D'Agostini, G. 1995, Nuclear Instruments and Methods in Physics Research A, 362, 487

Dermer, C. D. 2007, ApJ, 659, 958

Eddington, Sir, A. S. 1940, MNRAS, 100, 354

Faucher-Giguere, C., & Loeb, A. 2009, ArXiv e-prints

Fichtel, C. E., Hartman, R. C., Kniffen, D. A., Thompson, D. J., Ogelman, H., Ozel, M. E., Tumer, T., & Bignami, G. F. 1975, ApJ, 198, 163

Fields, B. D., Pavlidou, V., & Prodanovic, T. 2010, ArXiv:1003.3647

Gabici, S., & Blasi, P. 2003, Astroparticle Physics, 19, 679

Hartman, R. C., et al. 1999, ApJS, 123, 79

Hasinger, G., Burg, R., Giacconi, R., Hartner, G., Schmidt, M., Trumper, J., & Zamorani, G. 1993, A&A, 275, 1

Hopkins, A. M., & Beacom, J. F. 2006, ApJ, 651, 142

Inoue, Y., & Totani, T. 2009, ApJ, 702, 523

Inoue, Y., Totani, T., & Ueda, Y. 2008, ApJ, 672, L5

Jungman, G., Kamionkowski, M., & Griest, K. 1996, Phys. Rep., 267, 195

Keshet, U., Waxman, E., Loeb, A., Springel, V., & Hernquist, L. 2003, ApJ, 585, 128

Loeb, A., & Waxman, E. 2000, Nature, 405, 156

Makiya, R., Totani, T., & Kobayashi, M. A. R. 2010, ArXiv:1005.1390

Marcha, M. J. M., Browne, I. W. A., Impey, C. D., & Smith, P. S. 1996, MNRAS, 281, 425

Miniati, F. 2002, MNRAS, 337, 199

Mücke, A., & Pohl, M. 2000, MNRAS, 312, 177

Narumoto, T., & Totani, T. 2006, ApJ, 643, 81

Pavlidou, V., & Fields, B. D. 2002, ApJ, 575, L5

Pfrommer, C., Enßlin, T. A., & Springel, V. 2008, MNRAS, 385, 1211

Reimer, O., & Thompson, D. J. 2001, in International Cosmic Ray Conference, Vol. 6, International Cosmic Ray Conference, 2566

Sreekumar, P., et al. 1998, ApJ, 494, 523

Stecker, F. W., & Salamon, M. H. 1996, ApJ, 464, 600

Stocke, J. T., Morris, S. L., Gioia, I. M., Maccacaro, T., Schild, R., Wolter, A., Fleming, T. A., & Henry, J. P. 1991, ApJS, 76, 813

Strong, A. W., Moskalenko, I. V., & Reimer, O. 2004, ApJ, 613, 956

Thompson, T. A., Quataert, E., & Waxman, E. 2007, ApJ, 654, 219

Ullio, P., Bergström, L., Edsjö, J., & Lacey, C. 2002, Phys. Rev. D, 66, 123502

Urry, C. M., & Padovani, P. 1995, PASP, 107, 803

Wilks, S. S. 1938, Ann. Math. Stat., 9, 60